Abstract In this paper we review recent progress in obtaining laser action from semiconductor quantum cascade structures covering the low THz region of the electromagnetic spectrum, from 2 THz ($\lambda \simeq 155\,\mu$m) down to the sub-THz region ($\lambda > 300\,\mu$m). Particularly, laser active region designs based on bound-to-continuum transition and magnetically assisted intra-well transition are presented. The wide scalability of active region designs is discussed and illustrated with experimental data. Latest results including the demonstration of laser action from quantum heterostructure at 950 GHz are presented.

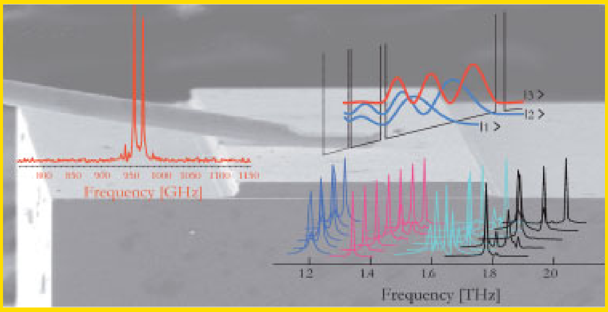

THz quantum cascade lasers are based on semiconductor heterostructures and cover a wide spectral window which now extends below 1 THz.

THz and sub-THz quantum cascade lasers

Giacomo Scalari[1,*], *Christoph Walther*[1], *Milan Fischer*[1], *Romain Terazzi*[1], *Harvey Beere*[2], *David Ritchie*[2], *and Jérôme Faist*[1]

[1] Institute of Quantum Electronics, Eidgenossische Technische Hochschule Zurich, Zurich, Switzerland
[2] Cavendish Laboratory, University of Cambridge, Cambridge, UK

Received: 4 July 2008, Revised: 19 August 2008, Accepted: 22 August 2008

Key words: Terahertz, laser, intersubband, low frequency, keywords.

1. Introduction

The THz region of the electromagnetic spectrum, which bridges the optical and radio-frequency domains represents a frontier area for research in physics, chemistry, biology, materials science and medicine. Many of the phenomena related to the mentioned domains have their typical energies and/or frequencies lying in the THz region. Emission from interstellar dust clouds [1], physical processes as highly-excited atomic Rydberg transitions, electrons in semiconductors and their nanostructures, superconducting energy gaps are all lying in the THz region. In applications, THz radiation is at the center of the interest for its potential in non-invasive imaging, applicable in different domains from medical diagnostics to homeland security scanners [2]. The components for such a THz photonics systems are objects of active research. We concentrate our efforts on the realization of narrow band THz sources exploiting the band-structure engineering in semiconductor heterostructures. We realize Quantum Cascade (QC) lasers, which are based on electronic transitions in the conduction band of a semiconductor heterostructure. Quantum confinement and resonant tunneling are used as key ingredients to achieve optical gain and laser action in the Mid and Far Infrared regions of the electromagnetic spectrum.

After the first demonstration at Bell labs in 1994 [3] QC lasers improved their performance and cover now a considerable portion of the electromagnetic spectrum. In the Mid-IR region impressive performance have been reached in terms of operating temperature [4], emitted powers and tunability [5]. The realisation of QC lasers in the THz region is more challenging because the energy of the photon is lower than the longitudinal optical (LO) phonon of the host material ($\hbar\omega_{LO} \simeq 36$ meV for GaAs) and because of free carrier absorption which scales with λ^2, heavily affecting the waveguide losses. The physics of the intersubband (ISB) transitions for such low energy spacing where optical phonon emission is forbidden at low temperatures

---

[*] Corresponding author: e-mail: scalari@phys.ethz.ch

is still the object of active research and the assessment of electronic state lifetimes and dephasing rates constitutes a challenging task.

Nevertheless, laser action has been demonstrated to-date from 5 THz down to 950 GHz (this work), with pulsed operation up to 178 K [6,7]. The lower portion of the THz spectrum is especially interesting for long-range standoff imaging [8], since the atmospheric transmission shows two wide spectral windows centered at 1.5 THz and 850 GHz (see for example the Hitran database). Another interesting application for lasers emitting in the low THz region is represented by the local oscillators in the heterodyne detection for radio astronomy [9, 10] where the QCL can represent a significant improvement over up-converted microwave sources. The QC lasers are typically realized by using Molecular Beam Epitaxy (MBE) for the growth of the heterostructure. In the last few years, Metal-Organic Vapor Phase epitaxy (MOVPE) has also proven to be a viable growth technique showing very good results in the Mid-Ir and also promising results in the realization of THz devices [11]. Since its first demonstration [12] several active region designs have been presented that reached laser action at THz frequencies [6]: in this paper we will concentrate on two designs developed in our laboratory, which allowed to demonstrate laser action at long wavelengths ($\lambda > 150\,\mu\mathrm{m}$) exploiting bound-to-continuum and intra-well transitions. General considerations on the design and the architecture of the active regions for THz QC lasers are discussed in Sect. 2. The choice of the optical resonator is also critical: the different waveguides employed in THz QCLs are summarized in Sect. 3. In Sect. 4 the bound-to-continuum with split injector design is discussed together with experimental data covering the wavelength range from 2.0 THz to 1.2 THz. In Sect. 5 the intra well structure with magnetically assisted gain are discussed with data demonstrating laser action in the sub-THz region. Sect. 6 summarizes the results achieved and discusses future developments concluding the paper.

2. Gain medium design

In this Section we discuss some general guidelines which led to the two active region designs described in Sect. 4 and 5. The main challenges in realising long wavelength THz quantum cascade lasers are essentially three: a selective and efficient injection of electrons in the upper state of the lasing transition and the achievement of optical gain between the subbands via population inversion while minimizing waveguide losses. The energy spacing between radiative states is lower than 8 meV (2 THz), and the physical mechanisms governing the electron dynamics in the subbands for this low energy spacing are not yet clear. The model that we employ to describe the electronic states in the conduction band is an “effective” one band model which includes non-parabolicity via an energy-dependent effective mass [13]. The effect of the doping is taken into account by solving self-consistently the coupled Schroedinger and Poisson equations. The material system which has proven to be the most successful is the GaAs/AlGaAs with different Al alloys. InGaAs/AlGaAs/InP THz lasers have been also demonstrated [14], but for the moment their performance is still inferior to the GaAs based ones. One module of the heterostructure can be described as the active region, which contains the states involved in the radiative transition, and the injector region, where the electrons thermalize and where the doping is located (see Fig. 1a).

Our modeling strategy is based on two main assumptions: the electron transport is coherent at the injection barrier and the electrons are thermally distributed in the injector region. Although the electronic temperature can differ significantly from the lattice one in the lasing states, as discussed in Ref. [15], we believe that the majority of the carriers reside in the injector where they are thermally distributed with an average temperature slightly higher than the lattice one. The current-voltage characteristics of the laser, in a crude approximation, can be modeled with a two-level density matrix approach, as described for a superlattice in the pioneering paper from Kazarinov and Suris [16], and then adapted to the quantum cascade laser by Sirtori et al [17]. In this model the two levels considered are the ground state of the injector and the upper lasing state. More refined models for transport and gain calculations make use of nonequilibrium Green’s functions [18], density matrices extended to extraction states too [19] and hybrid aproaches which include Monte Carlo [12] and coherence effects [20]. Using the same symbols as in Ref [17] the current density in the structure as a function of the applied electric field E can be written as:

$$J = qn_s \frac{2\Omega^2\tau_\perp}{1+\Delta^2\tau_\perp^2+4\Omega^2\tau_\perp\tau_{\mathrm{up}}} \qquad (1)$$

$$\text{where} \quad \Delta = q/\hbar(F-F_r)(z_{\mathrm{up}}-z_g) \qquad (2)$$

where F is the applied electric field, F_r is the resonant field at which states $|g\rangle$ and $|\mathrm{up}\rangle$ anticross, $2\hbar\Omega$ represents the energy splitting of the injector-upper state doublet, τ_{up} is the upper state lifetime and $\tau_\perp$ represents the intra-subband dephasing time and z_i is the center of mass of the electronics wavefunction (see Fig. 1). The J-V curve has then a Lorentzian profile, and the term that governs the injection process is $4|\Omega|^2\tau_{\mathrm{up}}\tau_\perp$. When this term is much greater than unity, the laser is in its optimal regime because the injection in the upper state is not limited by the tunneling rate but controlled by the upper state lifetime τ_{up} [17]. In this regime we can write the maximum current flow across the barrier as $J_{\max} = \frac{q_0 n_s}{2\tau_{\mathrm{up}}}$: the maximum current is controlled by the doping and the overall upper state scattering rate. The injection barrier represents a key parameter in a quantum cascade laser: its thickness results from a tradeoff between the optimal injection of carriers in the upper state and the parasitic coupling prior to the alignment. The current flow necessary to bring the ground state of the injector close to resonance with the upper lasing state represents a leakage current.

In THz QCLs, the expression $4|\Omega|^2\tau_{\rm up}\tau_\perp$ contains only one quantity that is directly adjustable by quantum design, the energy splitting $2\hbar|\Omega|$ between injector and upper lasing state. The upper state lifetime $\tau_{\rm up}$ which is reliably calculated for a Mid-Ir transition (LO phonon scattering dominates the lifetime) is not directly computable for a THz transition[1] but can be determined *a fortiori*.

The other parameter controlling the injection process is the intra-subband dephasing time. This quantity is strongly related to the growth parameters and to the nature (delocalized, localized) of the wavefunctions and is difficult to access experimentally. The intra-subband dephasing time can be written as [20]:

$$\frac{1}{\tau_\perp} = \frac{1}{2\tau_{\rm up}} + \frac{1}{2\tau_{\rm dn}} + \frac{1}{\tau_{\rm deph}}$$

where $\tau_{\rm deph}$ accounts for the pure dephasing in the density matrix model. If we assume homogeneous broadening (recent experiments suggest inhomogeneous broadening for some structures [21]), a good estimation of such intra-subband dephasing is offered by the spontaneous emission linewidth $2\gamma_{ij}$, which can be written (in energy units) [20, 22]:

$$2\gamma_{ij} = \hbar\left(\frac{1}{\tau_{\rm up}} + \frac{1}{\tau_{\rm dn}} + \frac{2}{\tau_{\rm deph}}\right). \qquad (3)$$

Typically, for transitions below the LO phonon energy, $\tau_{\rm up}$, $\tau_{\rm dn} \gg \tau_{\rm deph}$ and then we can deduce $\gamma_{ij} \approx \frac{\hbar}{\tau_\perp}$. Since the measured widths of low energy THz ISB transitions lie in the 1.5–0.5 meV range, the typical splittings at the injection resonance will also be tuned in the 1.3–0.2 meV range. It is clear that such small energy separations (corresponding to Rabi frequencies of some hundreds of GHz) pose severe constraints on the accuracy of the growth and of the band-bending effects which are related to the dopant ions present in the structure (see Sect. 4.1). Typical current densities flowing in THz QCLs are around 0.6–1 kA/cm^2 and the average doping of one period of the structure is of the order of 1–5 × 10^{15} cm^{-3}. In the case of low photon energies, the reduced coupling at the injector, for the same sheet carrier density n$_s$, implies reduced values for the J$_{\rm max}$ and for the injected current: this is in fact what is observed generally in long wavelength THz QC lasers [23–25]. In a simple, one-particle model the optical gain at the wavelength λ between the subbands i, j is expressed by the formula [26]:

$$G_p = \frac{4\pi e^2}{\epsilon_0 n_{\rm eff}\,\lambda\, 2\gamma_{ij}\, L_p} z_{ij}^2 (n_i - n_j) \qquad (4)$$

where z_{ij} is the dipole matrix element between radiative states, L_p is the length of one period of the structure and

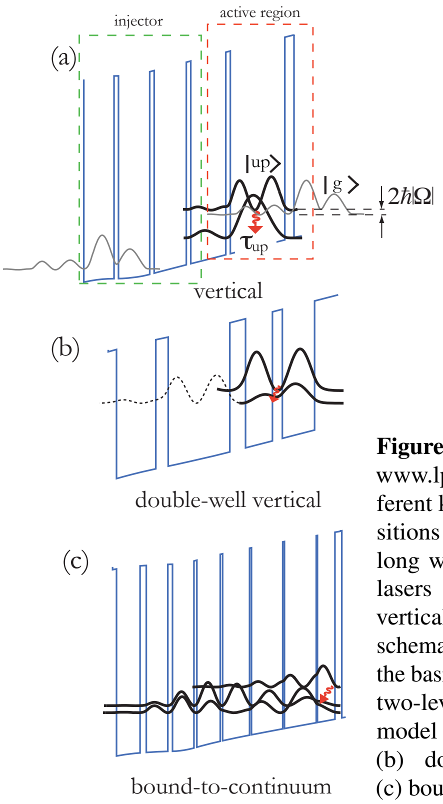

Figure 1 (online color at: www.lpr-journal.org) Different kinds of optical transitions in employed in long wavelength THz QC lasers (a) intra-well or vertical transition: on the schematic are reported also the basic parameters for the two-level density matrix model described in Sect. 2. (b) double-well vertical (c) bound-to-continuum

n$_{i,j}$ are surface densities. The term at the left of the population difference $n_i - n_j$ is usually called *gain cross section* and denoted with g$_c$ [26]. More refined models for the gain have been developed [27]: one of them includes also second order effects that can be important in low population inversion structures [28] and can also affect transport characteristics. Recently developed experimental techniques based on THz time domain spectroscopy will be extremely useful in the validation of the different gain models [29].

The resulting gain depends heavily on the type of wavefunctions: the main scattering mechanisms effective at low THz frequencies are represented by interface roughness and impurity scattering [22]; we recall that the typical doping density in or structures is in the 2–5 × 10^{10} cm^{-2} range, which reduces the efficiency of e-e scattering in affecting level lifetimes. Vertical transitions in real space generally present a narrower linewidth; delocalized transitions in real space have a broader linewidth (mainly affected by interface roughness) (see Fig. 1b,c). The most successful design for high temperature operation is the one based on a two-well active region with resonant-phonon depletion of the lower state in a three [30] or four well structure [6] (Fig. 1b). This kind of design seems however to be limited in the low frequency operation by the leakage current prior to the correct alignment of the structure [24].

Our results at long wavelength are obtained with two different optical transitions: in Sect. 4 a bound-to-continuum transition is employed. Such a transition involves one quantum state delocalized over three or four quantum wells

---

[1] For THz energy spacings, the emission of an LO phonon is energetically forbidden at $T = 0$ and therefore the scattering time depends on the electronic temperature of each subband, requiring a very complex calculation over the whole structure for the evaluation.

that are coupled to a lower quasi-miniband. It has in general a lower oscillator strength with respect to intra-well transitions or superlattices and the emission frequency can be tailored by acting on the first well width and adjusting the coupling with the other wells. The other approach, described in Sect. 5 is based on the use of a single quantum well for the active region and on the gain enhancement derived from the application of a magnetic field perpendicular to the plane of the layers.

As the photon energy is lowered, the cross absorption at the lasing frequency between injector states poses severe constraints to the achievement of gain. To circumvent this problem the injector can be modified either reducing the number of states [24] or by chirping the superlattice in order to minimize dipoles at the resonant frequency [23]. The active region design becomes then also a “loss” design: the waveguide core is not anymore modeled as a quasi-bulk GaAs doped with the average doping of the active region but the heterostructure states have to be considered. The band-structure engineering approach can be used also in this respect by suitably designing a low-absorption injector. We will describe in detail the solution that we adopted and which is based on a “split-injector” approach in Sect. 4. In the case of the magnetically assisted gain the cross-absorption in the injector is reduced by the narrowing of the states due to the magnetic confinement.

3. Waveguides

The low photon energies of our structures correspond to wavelengths longer than 150 µm in vacuum. Traditional dielectric waveguides are unpractical because of the large cladding thickness required; solutions relying on the use of metallic layers supporting surface plasmon modes have been developed for an efficient guiding of the THz radiation Two principal schemes have been developed to provide efficient optical resonators for THz QCLs: single plasmon and double metal waveguides. Based on these two main waveguides configurations, more refined structures have been realized where photonic bandstructure engineering is implemented [31–35].

3.1. Single plasmon waveguide

This waveguide represented the key ingredient in the demonstration of the first THz QCL [12, 36]. The confinement of the electromagnetic wave is based on a metallic reflection at the top metallization and the quasimetallic confinement provided by a thin, heavily doped buried contact placed below the heterostructure. A two dimensional calculation of the mode intensity is reported in Fig. 2a. The heterostructure has to be grown on a semi-insulating substrate. In this way the large part of the mode which overlaps with the substrate brings a very small contribution to the waveguide losses. The heavily doped (typically

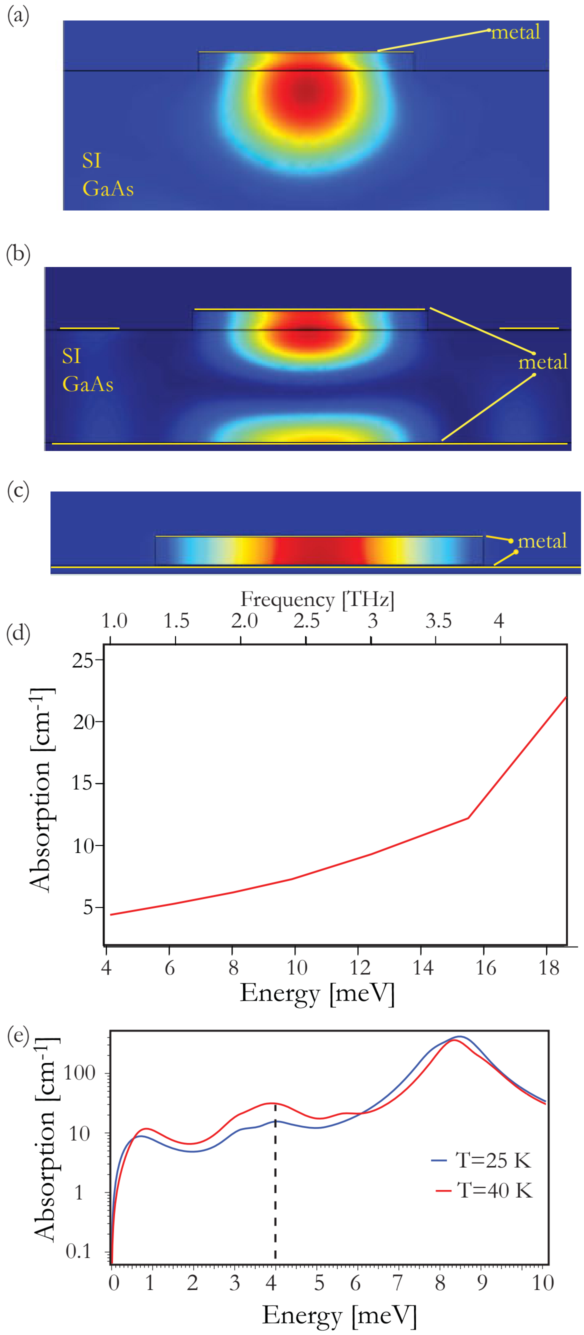

Figure 2 (online color at: www.lpr-journal.org) (a) computed mode intensity for a single plasmon waveguide at 3 THz (200 µm wide, 17 µm thick). (b) computed mode intensity for a 200 µm wide, single plasmon waveguide at 1.9 THz with a 600 nm thick buried layer: note the double lobed mode; the figure of merit is $\Gamma = 0.22$ and $\alpha_w = 8\,\text{cm}^{-1}$. (c) computed mode intensity for an “empty” double-metal waveguide 200 µm wide and 17 µm thick at 950 GHz. (d) calculated absorption for the empty waveguide of point (c) as a function of photon energy. The parameters used for the metals are measured at 300 K and are reported in Ref. [40] (e) intersubband absorption calculated at two different temperatures for the active region of sample A3913 of Sect. 5. The dashed line is the photon energy.

0.8–2 × 10^{18} cm^{-3}) buried layer has the double function of optically confining the mode and acting as an electrical contact. Because of the large and negative dielectric constant of the buried contact, the overlap factor between the field and this heavily doped region is very small. The main advantage of this waveguide resides in its quite high figure of merit (overlap divided by losses) in the 2–4 THz region associated to a facet reflectivity still close to the Fresnel one calculated via index mismatch [37] eases the coupling to free space modes and yields a good far-field. This waveguide loses its efficiency as the photon energy is lowered: the longer wavelength has to accommodate the same epilayer thickness and the reduction of the dielectric constant of the active region pushes the mode towards the substrate reducing the overlap. Another general disadvantage of this waveguide is the non-optimal and non uniform ridge pumping due to the injection via the buried layer which shows significant in-plane resistance [38]. One possibility to still keep the single plasmon configuration at long wavelength is to rely on a mode which is bounded to the two metallic layers which constitute respectively the top contact and the back metallization of the sample. If the semi-insulating substrate is properly thinned down to a thickness of about a 100 µm (the optimal thickness is wavelength dependent), the mode with the highest figure of merit is the one depicted in Fig. 2. In this way the active region still experiences a good overlap with the optical mode even if one big part of it is "pulled" towards the lower metallization layer. This waveguide configuration has been successfully employed in the 1.9 THz laser of Ref. [39] and in the devices of Refs [23] (2 THz) and [25] (1.6–1.8 THz). In fact this configuration represents an "hybrid": the two metals guide the radiation as in a double-metal waveguide described here below.

3.2. Double metal waveguide

The double metal waveguide is directly derived from the microstrip resonator widely employed in the microwave range. In this waveguide the active region is sandwiched between two metallic layers, typically Au, yielding an almost unity overlap factor. It has been first demonstrated in QCL at Mid-IR frequencies [41] and then widely employed in combination of resonant-phonon designs in the devices that have shown the highest temperature performance to-date [6]. Recently, Cu has been proficiently used to enhance the figure of merit of this waveguide setting the new limit in pulsed high temperature operation [7]. The main disadvantage of this waveguide is represented by the patterned far-field [10] due to the impedance mismatch at the laser facet: solutions based on micro-lenses [42] or horn antennas [43] which show substantial improvement in the collected power have been developed. As the frequency is lowered the figure of merit of this kind of waveguide remains almost constant: the free carrier absorption scales as λ^2 [44] (and can be partially engineered by the injector design)but the losses due to the metallic layers improve because the metals behave more and more as perfect conductors. In Fig. 2c is plotted the two-dimensional simulation of the mode intensity for a double metal resonator at 950 GHz. The waveguide losses are calculated considering the waveguide core as an undoped bulk and then adding separately the contribution of the intersubband absorption calculated by thermally populating the heterostructure at the operating bias. The losses are then design-dependent. As an example, for the 950 GHz structure presented in Sect. 5 we obtain total waveguide losses of $\alpha_w^{\text{tot}} = \alpha_w^{\text{empty}} + \alpha_{\text{ISB}}^{T=25\,K} = 4.5 + 14 \approx 19\,\text{cm}^{-1}$. The waveguide losses are also temperature-dependent: the optical figures of the metals slightly degrade with temperature [7] and the thermal population of the injector states can increase the intersubband absorption.

4. Bound-to-continuum with split injector

4.1. Active region design

The bandstructure, shown in Fig. 3a, is based on a bound-to-continuum transition [45, 46] with an energy gap that splits the miniband from the two injector states. The advantage of the bound-to-continuum scheme is the large

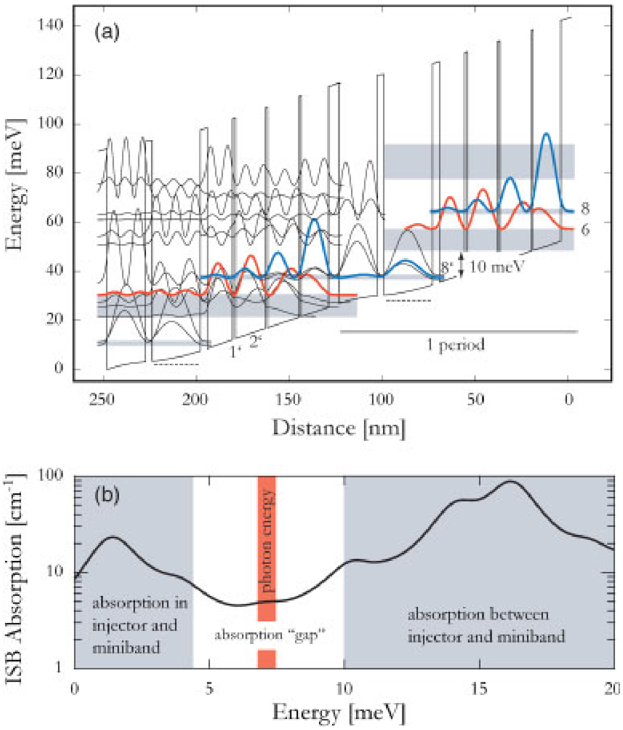

Figure 3 (online color at: www.lpr-journal.org) (a) Self-consistent solution of coupled Schroedinger and Poisson's equations for an applied electric field of 2.25 kV/cm. A dashed line is indicating the Si-doped layer, $1.0 \cdot 10^{16}$ cm^{-3} in density. The nominal doping level yields a sheet carrier density of $2.6 \cdot 10^{10}$ cm^{-2} and an average doping density of $2.1 \cdot 10^{15}$ cm^{-3}. (b) Calculated intersubband absorption spectrum assuming a thermal equilibrium distribution of the carriers ($T = 50$ K) .

phase space for scattering out of the upper and lower states. By considering only interface roughness scattering [22], a population inversion between the upper and lower state is predicted at low temperature [47]. Although interface roughness scattering may be the dominant diffusion mechanism of the upper state, other scattering mechanisms such as electron-electron [48] and electron-impurity scatterings are supposed to contribute significantly to the extraction of electrons from the lower state, which is part of the miniband, leading to a even larger predicted population inversion.

An energy gap splits the injector states from the miniband, allowing a well controlled injection process and reducing the possibility of backfilling. The two injector states are off-resonance prior to the alignment with the upper state, which reduces efficiently the parasitic current from the injector in the miniband. At injection resonance with the upper state, the injector states themselves are also in resonance, leading to a high injection efficiency in the upper state.

Intersubband absorption at the photon energy is minimized by bandstructure engineering that allows one to transfer the oscillator strength of the injector absorption on energies above the photon energy by means of the energy gap. Fig. 3b shows the calculated intersubband absorption at 50 K for the bandstructure of Fig. 3a with the assumption of a thermal equilibrium distribution of the electrons. Two highly absorbing regions above and below the photon energy are separated by an absorption gap that originates from the introduction of the energy gap between injector states and the miniband, which is larger than the photon energy.

4.2. Devices characterization

The low frequency bound-to-continuum lasers which are described here were all grown by MBE on GaAs substrates. 85–120 repetitions of the active region sandwiched between two highly doped contact layers give a total growth thickness of (13–17 µm). Samples were processed by wet etching in a double metal waveguide with non-alloyed Ti/Au contacts, then cleaved, indium soldered on copper mounts and measured on the cold finger of a helium flow cryostat.

The low frequency bound-to-continuum lasers show a strong Stark-shift of the gain curve with the voltage, which reveals the diagonal nature of the transition and a relatively low ratio of the upper to lower state lifetime $\tau_{\mathrm{up}}/\tau_{\mathrm{dn}}$ [49]. A large ratio of the lifetimes would lead to a photon controlled transport with pinning of the bias voltage above threshold and no significant Stark-shift [50]. Fig. 4 shows the $L-I$ characteristics of a sample of structure N891, grown with the bandstructure of Fig. 3. At 10 K the maximal cw power is 1.5 mW. Operation is observed up to 60 K in the continuous wave (cw) mode. The highest operating temperature for a device of structure N891 is 100 K in pulsed mode at a low duty cycle (0.12%). Continuous wave laser spectra are reported in the inset of Fig. 4 for two different biases. Lasing occurs on Fabry-Pérot modes of the cavity. At higher temperature, the dynamic range of the laser becomes smaller, due to a higher threshold current density. With a smaller dynamic range, the tuning range of the gain gets reduced, starting from the low frequency side. At the highest operating temperature the laser is lasing at the highest frequency.

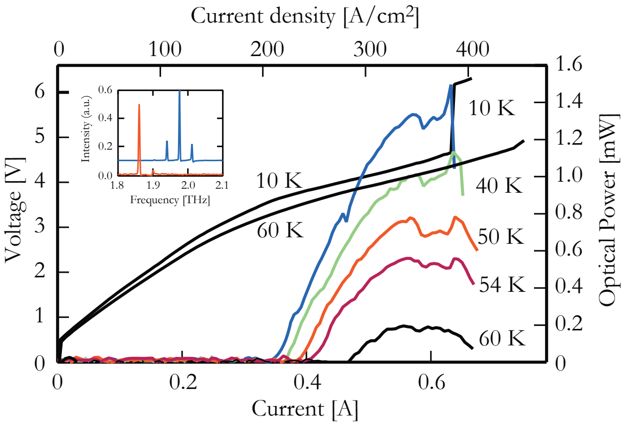

Figure 4 (online color at: www.lpr-journal.org) cw $L-I$ characteristics of a 1 mm long and 165 µm wide sample of the structure N891. The voltage-current characteristics at 10 K and at 60 K are shown. For the power measurement an absolute Terahertz power meter was used (Thomas Keating Instruments) in combination with a mechanical chopper at 30.3 Hz. The light is collected and guided to the power meter with a straight cone. The inset shows spectra at two different biases. The devices of the layer N891 are lasing between 1.8 and 2.1 THz.

4.3. Scaling of the bandstructure

Rescaling of the bandstructure of Fig. 3a from 2.0 THz ($h\nu \sim 8$ meV) to frequencies as low as 1.2 THz ($h\nu \sim 5$ meV) has been achieved. We rescaled the energy spacing between the states by keeping the same shape of the wavefunctions. Special care has been taken for quantum states which are lying close in energy and where the electron transport is dominated by resonant tunneling [17], which is the case for the two injector states and the upper state at alignment bias. In this case the energy splitting between the individual states is kept identical. At low photon energy, the doped injector well cannot be narrowed sufficiently by keeping the coupling scheme of its excited state with the miniband and bringing the two injector states in resonance at the alignment bias. Therefore, the doping scheme has been changed for the bandstructure designs below 1.6 THz with the benefit that the average potential drop between the two injector wells is increased, enabling a proper alignment of the two injector states at alignment bias, as shown in Fig. 5.

Drawbacks of this doping scheme are that the dopants are lying closer to the active region, which increases the possibility of broadening of the upper state due to ionized impurity scattering [51]. Furthermore the alignment of the

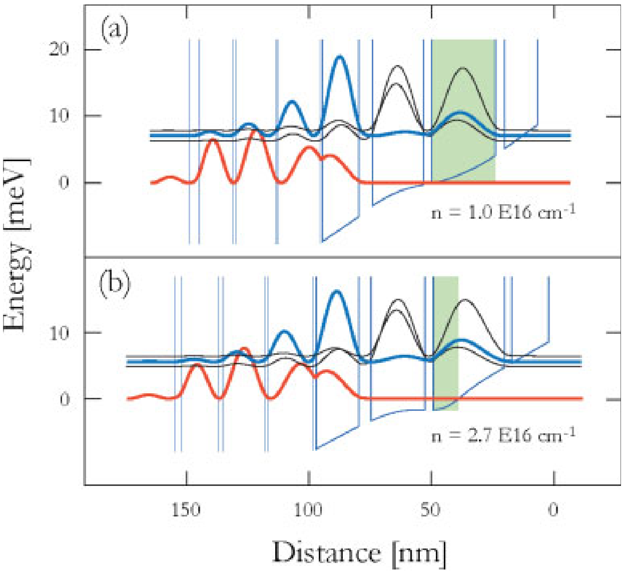

Figure 5 (online color at: www.lpr-journal.org) Comparison of the injector region of the (a) 2 THz design (layer N891) and (b) the 1.5 THz design (layer N892). The 1.5 THz design has a different doping scheme, which is higher in density, but only a fraction of the well is doped, leading to the same nominal sheet carrier density.

injector states and the upper state are more sensitive on variation of the nominal doping during growth and depends on the electron distribution in the quantum states.

Table 1 Summary of some characteristics of the four bound-to-continuum lasers with split injector. Calculated values and design parameters are shown above, measured and deduced values below.

Layer	N891	N899	N892	N908
Energy splitting $2\hbar\Omega$, meV	0.67	0.67	0.63	0.54
Thickness of AR, µm	14.2	15.9	12.1	12.2
Number of periods	110	2×60	85	85
Period length, nm	122.8	126.8	134.7	135.7
Oscillator strength	18.9	18.9	17.3	16.6
Carrier density, 10^{10} cm^{-2}	2.6	2.2	2.7	2.7
Avg. doping, 10^{15} cm^{-3}	2.1	1.7	2.0	2.0
Facet Reflectivity	0.80	0.80	0.86	0.88
$\alpha_{\mathrm{ISB}}^{T\,=\,50\,\mathrm{K}}$, cm^{-1}	12.0	10.5	14.9	15.0
$\alpha_w^{\mathrm{empty}}$, cm^{-1}	8.3	8.3	10.3	9.5
W.guide losses α_w^{tot}, cm^{-1}	20.3	18.8	25.2	24.5
Mirror losses, L=1 mm, cm^{-1}	2.2	2.2	1.5	1.3
Slope efficiency, mW/A	7.2	7.1	2.0	1.7
Threshold current, A/cm^2	203	144	289	293
Maximum current, A/cm^2	380	273	426	341
Dynamic range	0.46	0.47	0.32	0.14
Average frequency, THz	1.9	1.7	1.5	1.3
Stark-shift of gain, meV	1.0	1.0	1.0	0.6
$T_{\max}$, K	100	97	84	69
Avg. doping, 10^{15} cm^{-3}	4.06	3.45	3.99	3.61
$R_{d,S>0}/R_{d,S=0}$	0.68	0.70	0.72	0.76
$\tau_{\mathrm{eff}}/(\tau_{\mathrm{eff}}+\tau_2)$	0.17	0.16	0.14	0.15

4.4. Frequency coverage

A systematic comparison of four different lasers which cover the frequency range from 2.1 to 1.2 THz will be presented. The lasers are labeled according to the grown layers: N891, N892, N899 and N908. These four lasers were grown during the same run with molecular beam epitaxy, which is an advantage for comparison, as background impurity doping and interface roughness of the lasers are comparable. The layer N899 is similar in design and performance to the layer V303 which was grown in a different chamber [25].

Laser N891 and N899 are based on the bandstructure with a uniformly doped injector well, scaled to the desired photon energy. A typical layer sequence is given in reference [25]. N899 is a bi-stack structure with the designed gain curves of the two stacks shifted by 0.6 meV. Laser N892 and N908 are based on the bandstructure with the fractionally doped injector well, the layer sequence is given in reference [47]. More details on the four lasers are listed in Table 1.

Fig. 6a shows an overview of cw spectra of the four lasers. For each laser different spectra were measured at different voltages. Although the gain curve of the lasers can be widely and continuously tuned by the Stark-shift, the lasing frequency is fixed by the optical modes of the cavity. The gain curve of each laser can be tuned in such a way that these four lasers cover together the frequency range from 2.1 to 1.2 THz. For the chosen dimensions of the cavities, the lasers N892 and N908 lase mostly on only one longitudinal cavity mode contrary to N899 and N891 which are multimode for most of the voltages. Higher lateral modes in N899 and N891 have low enough losses to lase due to the shorter wavelength.

4.5. Emitted power

In this part we compare the generated optical power as a function of frequency and discuss the slope efficiency's dependence on the laser parameters. Fig. 6b gives an overview on the measured power as a function of frequency of four lasers. The power was measured at 10 K in the cw mode. The optical cw power at 10K is only slightly lower than the peak power in pulsed mode. The power generated from each laser shows a strong frequency dependence due to the Stark-shift. The maximum powers of each laser are fitted with a straight line, giving a general tendency of lower achieved power at lower frequency which results from a combination of a smaller slope efficiency and a smaller dynamic range.

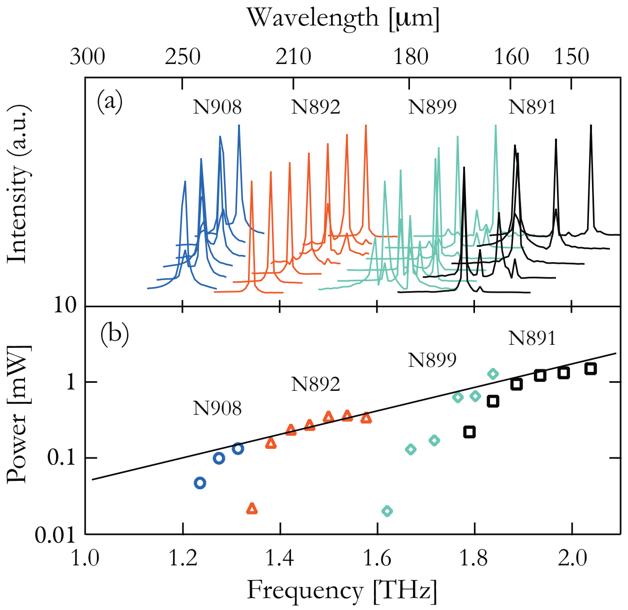

Figure 6 (online color at: www.lpr-journal.org) (a) Spectral characterization in the cw mode at 10 K of four devices. Spectra were measured for different applied bias. The devices are all 1 mm long, and 165 µm wide, except the one of N899 which is 110 µm wide. (b) Measured power of four lasers in cw mode at 10 K as a function of the frequency. All lasers are 1 mm long and 165 µm wide. For the power measurement on absolute terahertz power meter was used (Thomas Keating Instruments). The light is collected and guided to the power meter with a straight cone.

The slope efficiency describes the efficiency of generation of photons by pumping electrons through the laser and the out-coupling of the photons. For a waveguide with uncoated facets it is given by [38]

$$\frac{dP}{dI} = \frac{1}{2} N_p \frac{h\nu}{e} \frac{\alpha_m}{\alpha_w + \alpha_m} \frac{\tau_{\text{eff}}}{\tau_{\text{eff}} + \tau_2} \qquad (5)$$

where $\tau_{\text{eff}} = \tau_3(1-\tau_2/\tau_{32})$. In Table 1 the measured values of the slope efficiency for these lasers are listed. There is a difference by roughly a factor of 4 between the slope efficiencies of the lasers lasing above 1.6 THz and those lasing below 1.6 THz.

The slope efficiency is proportional to the photon frequency and to the number of periods. The lasers below 1.6 THz, N892 and N908, have significantly fewer periods, giving a lower slope efficiency also because of the lower photon energy. Fewer periods results also in a thinner active region, and due to the subwavelength-confinement of the mode to a larger impedance mismatch between waveguide and free space, leading to higher facet reflectivity and by consequence lower mirror losses [37]. In the considered regime of active region thickness and frequency, the slope efficiency has a strong dependence on the number of periods, but it is an easily adjustable parameter. For example the slope efficiency of N892 is expected to be 1.7 times larger by only growing 25 additional periods, which would result in a total thickness of 15.4 µm of the active region. Independently from the thickness of the active region in the considered range, the impedance mismatch between waveguide and free space remains very high, resulting the main limiting factor for the slope efficiency. For the whole set of devices the mirror losses are typically 10 times lower than the waveguide losses (Table 1). By improving the impedance matching (see Sect. 3.2), an order of magnitude higher slope efficiency could potentially be achieved with the same active region.

From the measured slope efficiency the ratio of the lifetimes $\tau_{\text{eff}}/(\tau_{\text{eff}}+\tau_2)$ can be deduced. The ratios of the lifetimes, listed in Table 1, don't show a significant decrease with the frequency.

The dynamic range affects the total power which is generated by a laser. It is given by

$$D_r = \frac{j_{\text{max}} - j_{\text{th}}}{j_{\text{max}}} \,. \qquad (6)$$

The dynamic range for N892 and especially for N908 are significantly smaller than those of N891 and N899 (Table 1), also contributing to the lower total power obtained for N892 and N908.

4.6. Temperature performance

The threshold current density of the four lasers as a function of the temperature is shown in Fig. 7a. All four lasers show a negligible increase of the threshold current density

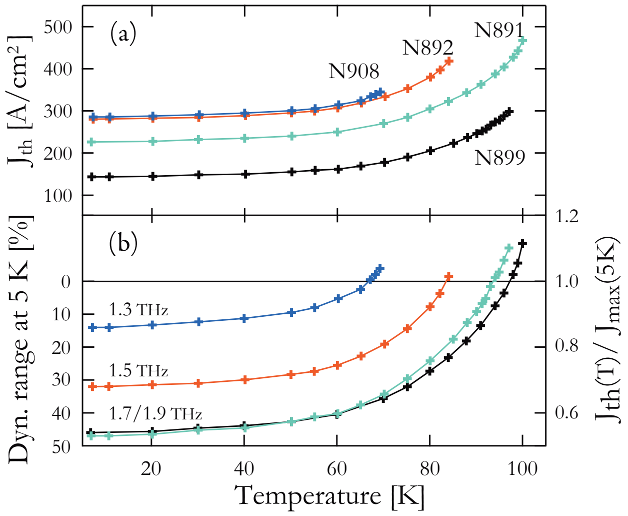

Figure 7 (online color at: www.lpr-journal.org) Temperature performance of four lasers. (a) Threshold current density as a function of temperature measured in pulsed mode at a very low duty cycle (0.12%). The lasing threshold was detected with a bolometer. (b) The threshold current density normalized by the maximum current density J_{max} at 5 K . The dynamic range at 5 K is displayed on the left axis.

up to 50 K, followed by a relatively strong increase up to the maximal operation temperature. The highest operation temperature of 100 K is reached by N891.

The threshold current density normalized to the maximal current at injection resonance $J_{\max}$ at 5 K is shown in Fig. 7b. It allows a more easy comparison among the four lasers which have different threshold current densities and dynamic ranges. The dynamic range at 5 K can be read on the left axis. The normalized threshold current density of the different lasers shows a similar increase with temperature. There is an apparent link between the dynamic range at 5 K and the maximal operating temperature. The graph suggests that the lower maximal operating temperature of the lasers at lower frequency is rather related to the smaller dynamic range at 5 K than to the lower photon energy. The maximal current $J_{\max}$ increases with the temperature therefore the normalized threshold current density exceeds unity at higher temperatures. At the highest operating temperature of N891 and N899, the maximal current $J_{\max}$ increases by about 12%, indicating that in these lasers the upper state lifetime decreases with the temperature (see Sect. 2).

The reason for the increase of the threshold current density with temperature is still not well understood and could be due to different mechanisms. Decrease of the upper state lifetime may be a reason, but also the broadening of the states could increase with temperature due to higher in plane scattering which would lead to a larger linewidth, lower gain cross section and a lower injection selectivity. The intersubband absorption and free carrier absorption might as well increase with the temperature.

4.7. Waveguide losses

Waveguide losses are calculated for the four lasers according to the description in Sect. 3.2. For the calculation of the intersubband absorption we used the doping values measured by capacitive measurements [52] and reported in Table 1. The measured average doping in the active region is about twice the intentional doping.

Fig. 8a shows the calculated waveguide losses for all four lasers. Due to loss engineering via the bandstructure and the waveguide, the losses do not show a λ^2 increase with the frequency, which would be expected if free carrier losses were dominating in the structure. There is still a slight, but not dramatic, increase of the losses with the wavelength.

The threshold current density depends on the waveguide losses. In a three level model the threshold current density is given by the following relation [26]:

$$J_{\text{th}} = \frac{e}{\tau_{\text{eff}}} \frac{\alpha_{\text{tot}}}{g_c} \qquad (7)$$

where the total losses α_{tot} are the sum of waveguide and mirror losses and g_c is defined in Sect. 2. Under the assumption of identical intersubband scattering times and linewidth of the spontaneous emission, the threshold current density J_{th} reads, $J_{\text{th}} \propto \alpha_w L_p / f_{\text{osc}}$, where α_w are the waveguide losses, f_{osc} the oscillator strength, and L_p the length of the period. The mirror losses are one order of magnitude smaller than the waveguide losses and were neglected. The computed values of $\alpha_w L_p / f_{\text{osc}}$ are compared in Fig. 8b to the measured threshold current densities, showing a good qualitative agreement. For the lasers below 1.6 THz a significantly higher threshold current density is predicted than for those above 1.6 THz, in full agreement with the measurement. The higher threshold is a combination of higher losses and lower oscillator strength, underlining the importance of optimizing the waveguide losses. However this simple model shows a qualitative discrepancy for the threshold current density of the lasers N891 and N899. We believe that this difference in the threshold current density of these two lasers is related to the injection efficiency, as discussed further in Sect. 4.9.

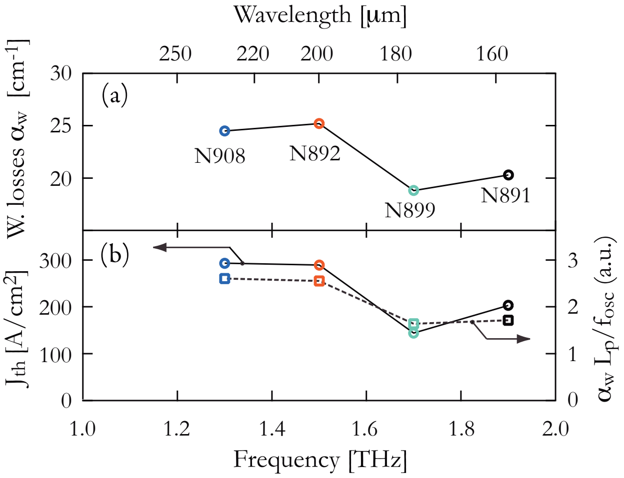

Figure 8 (online color at: www.lpr-journal.org) (a) Calculated waveguide losses α_w. (b) Comparison between the measured threshold current density (left axis) and the calculated expression $\alpha_w L_p / f_{\text{osc}}$ (right axis).

4.8. Lifetimes

The laser performance depends crucially on the lifetimes of the intersubband levels. Although lifetimes are not directly measurable, the lifetime ratio $\tau_{\text{eff}}/(\tau_{\text{eff}} + \tau_2)$, which represents the internal quantum efficiency of the laser transition, can be deduced from measurements. The slope efficiency is related to the internal quantum efficiency by the expression 5 and its value can bring informations on the lifetime ratio. Another possibility is offered by the measurement of the differential resistance. The ratio of the differential resistance above and below threshold is related to the internal quantum efficiency by the following equation [38]:

$$R_{d,S>0}/R_{d,S=0} = 1 - \frac{\tau_{\text{eff}}}{\tau_{\text{eff}} + \tau_2}\,. \qquad (8)$$

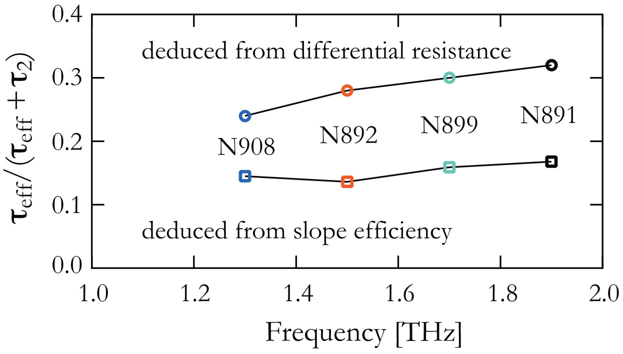

Figure 9 (online color at: www.lpr-journal.org) Deduced lower limit of the internal quantum efficiency at threshold, by the measurement of the slope efficiency and the change of the differential resistance at threshold.

Both methods allow to deduce a lower limit of the internal quantum efficiency, shown in Fig. 9. An additional series resistance would lead to an underestimation of the internal quantum efficiency by the technique of the differential resistance, whereas the non-unity collection efficiency of the power measurement setup leads to an underestimation by the technique of the slope efficiency. Taking the data obtained from the differential resistance as a reference, a power collection efficiency of 50% is estimated for the optical setup.

The relatively small ratio of the lifetimes may be related to a non unitary injection efficiency. For laser with extremely low values of the photon energy, the injection efficiency is not expected to reach unity in the upper state. However the injection efficiency is implicitly included in the values of τ_{eff} in this simple model.

The internal quantum efficiencies obtained by both methods are plotted in Fig. 9 and decrease as the laser frequency is lowered; the population inversion degrades. However the decrease is not dramatic and doesn't scale with the energy spacing between upper and lower state which varies from 8 to 5 meV for the considered lasers. Still a sizeable population inversion should be achievable at even lower frequencies if the injection selectivity is guaranteed.

4.9. Injection efficiency

The electronic injection efficiency in the upper lasing level is not accessible from a direct measurement. However a careful analysis of the lasers transport properties gives indications on the injection efficiency. Fig. 10a shows the I-V characteristics of the four lasers. The large discontinuity in the I-V characteristics is due to the region of negative differential resistance after the injection resonance [17]. The differential resistance in the low voltage regime is not very steep, especially for lasers N892 and N908, indicating

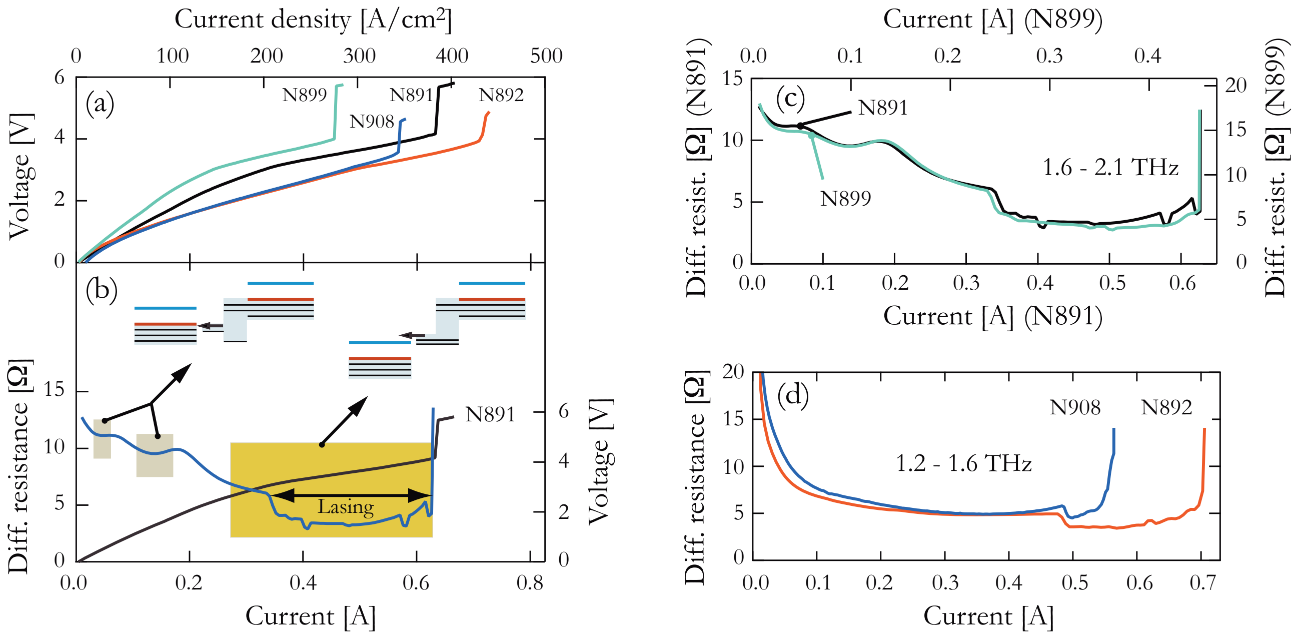

Figure 10 (online color at: www.lpr-journal.org) Comparison of transport properties of four lasers. The same lasers as in Fig. 6b have been used, the dimension of all lasers are 1 mm × 165 µm. (a) I-V curves of the lasers (a constant voltage drop due to Schottky barrier has been substracted). (b) I-V curve of N891 and its differential resistance, obtained by a differentiation of the I-V curve. Different transport regimes are identified. At low current, electrons are injected in miniband states, at higher current electrons are injected in the upper state. (c) Comparison of the differential resistance the laser N891 and N899 (corresponds to lasers from 1.6–2.1 THz) and (d) differential resistance of N892 and N908 (corresponds to lasers from 1.2–1.6 THz).

an strong electron transport through the structure prior to alignment.

The differential resistance is obtained by a differentiation of the I-V curve and is shown for sample N891 in Fig. 10b. The differential resistance reveals two humps in the low current regime due to injection resonances from the injector state to miniband states. The alignment of the injector state with the upper state starts after the second hump. In this picture, the injection efficiency in the upper state vanishes in the low current regime and increases only after the second hump.

Fig. 10c shows a comparison of the differential resistance of samples N891 and N899. To compare the two lasers, since each one has a different current density range, separate x and y-axis are used. The x-axis of N899 is scaled by 0.72 and accordingly, the y-axis by 1/0.72, compared to N891. The almost perfect overlap of the features in the differential resistance and threshold suggest nearly identical lifetimes and transport regimes in the two structures. Since the threshold current densities do not follow the prediction (see Fig. 8) we may argue that the threshold condition in this case is affected by the injection efficiency leading to voltage-controlled device [53]. This may explain the quite different threshold current densities displayed by these two lasers ($\mathrm{J}_{\mathrm{thresh}}^{N891} = 203\,\mathrm{A/cm}^2$, $\mathrm{J}_{\mathrm{thresh}}^{N899} = 144\,\mathrm{A/cm}^2$). The scaling factor for the current which is used in Fig. 10c is mainly due to the doping which is indeed 20% lower in N899 than in N891.

The differential resistances of the lasers below 1.6 THz, shown in Fig. 10d, look very similar. The lower maximal current density in laser N908 is related to the smaller energy splitting $2\hbar\Omega$ between the injector state and the upper state at injection resonance [47], and possibly also to the 10% lower doping in N908, resulting in a smaller dynamic range. The absence of humps together with the less steep I-V curves and lower differential resistance in the low current regime point towards a large non-resonant scattering channel from the injector state to the miniband prior to alignment. The overall injection selectivity of the injector is reduced in the lasers below 1.6 THz compared to the lasers above 1.6 THz. A gradual decrease of the injection selectivity with lower frequencies is expected due to lower energy spacings between the electronic states. However the very different transport properties of the lasers below 1.6 THz suggest that the abrupt decrease of the injection selectivity is rather related to the modified doping profile than to the downscaled energies.

Scattering of electrons with ionized impurities contributes significantly to the transport of electrons in THz QCL's [54]. Ionized impurity scattering depends strongly on the position of the impurities and their overlap with the wavefunctions [22]. The lasers below 1.6 THz, have only a fractionally doped second injector well. The modified doping profile may lead to different impurity scattering in the injector region. Larger scattering rates from the injector states would decrease the injection selectivity, leading to larger non-resonant currents prior to alignment and lower injection efficiency in the upper state at alignment bias. During the growth of the structures the dopants migrate in the growth direction resulting in a shift and smearing out of the doping profile [55]. The alignment of the bandstructure crucially depends on the self-consistent calculation of the potential with the nominal doping profile. A different effective doping profile may affect the proper alignment of the injector states.

Optimization of the injector region and doping profile for high injection selectivity and a large contrast of the current at injection resonance $J_{\max}$ to the current prior to alignment should lead to the demonstration of the 1 THz QC laser with this design approach.

5. Magnetically assisted gain in large quantum wells

5.1. Active region design

From the discussion in Sect. 2, one of the critical issues in dealing with low energy QCL is the level broadening which enters both in the gain expression as well as being one key element in the charge transport. The in-plane degree of freedom strongly affects the intersubband level linewidth; hence, the possibility to control the electron in-plane degree of freedom can provide an essential tool in order to gain insight into the physics of the system. This three dimensional confinement of the electron can be achieved, in a clean, direct and controlled way, by applying a strong magnetic field perpendicularly to the layers [56]. This will produce the breaking of the in-plane parabolic energy dispersion and the formation of discrete Landau levels allowing the creation of quasi-0D states [57]:

$$E_{|i,n\rangle} = E_i + \left(n + \frac{1}{2}\right)\frac{\hbar e B}{m^*} = E_i + \left(n + \frac{1}{2}\right)\hbar\omega_c\,. \tag{9}$$

The possibility to break the parabolic dispersion in the quantum well plane and eventually quench optical phonon emission [58, 59] is very attractive when trying to probe the ultimate threshold limit of quantum cascade devices.

We want to exploit the confinement effect in a twofold way: on one side we aim to achieve laser action at low THz frequencies with extremely reduced threshold current densities, to probe the limits of the intersubband lasers. The unique feature of the QC laser is that it is a unipolar device: in principle the system does not have a transparency current. This quantity is represented for the QCL by the current flow necessary to align the levels and to inject electrons in the upper lasing state [53]. Laser threshold is then determined entirely by the cavity losses. The THz transitions forbid the LO phonon emission at low temperatures: a further reduction in the number of states available for scattering represented by the magnetic confinement can then allow to obtain very long electronic lifetime in the subbands. The laser action will then be possible with extremely reduced thresholds, of the order of a few A/cm^2. On the other side a

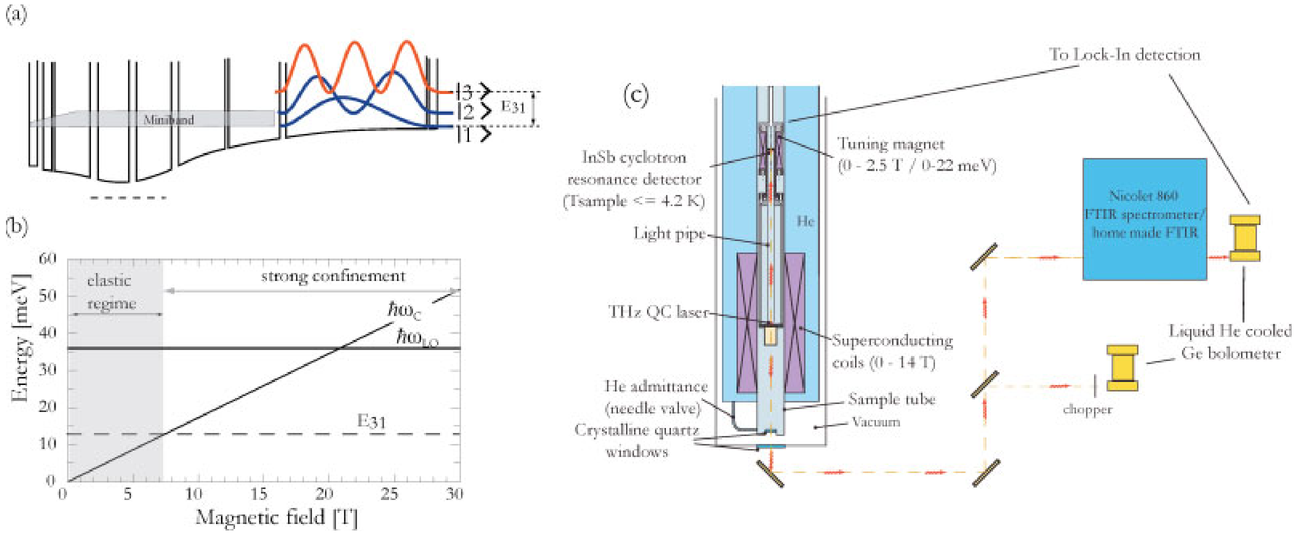

Figure 11 (online color at: www.lpr-journal.org) (a) Design scheme for the magnetically assisted gain samples emitting from 3.6 THz down to 1.39 THz. The large quantum well levels are tuned to satisfy $E_{32} = \frac{3}{2}E_{21}$. The underlined layers are the doped ones. The structures are realized in the $\mathrm{Al}_{0.15}\mathrm{Ga}_{0.85}$As/GaAs material system (b) Energy scales for lasers in magnetic field. (c) Magnetic field measurement setup: radiation path is marked with dashed lines and wavy arrows

detailed magneto-spectroscopy [60] of the active region of the laser can be carried out, yielding important informations on energy levels position and scattering mechanisms. In presence of this additional confinement, the intersubband scattering rate strongly depends on the respective energies of the Landau levels associated with the separate subbands. Because of short range disorder caused by interface roughness [61], this scattering rate will greatly increase whenever two Landau levels with different indices associated with separate subbands of energy E_i and E_j are in resonance, i.e. when the condition:

$$\Delta E_{ij} = \delta n \hbar\omega_c \tag{10}$$

is satisfied for an integer δn. In contrast, when the Landau level ladders are off resonance, the scattering rate will be minimized. Such modulation of lifetimes by these resonances has been demonstrated experimentally in electroluminescence measurements in ISB THz emitters [62, 63] and lasers [64, 65].

Our design for exploiting the magnetically assisted gain is kept very simple: the active region is constituted by a wide quantum well and the optical transition (intra-well) takes place between the second $|3\rangle$ and first $|2\rangle$ excited states. Resonant tunneling is exploited to increase population inversion at zero applied field [19]. A superlattice injector with a funnel-like energy dispersion bridges the periods and contains the doping, as schematized in Fig. 11a. The overall energy dispersion of one active well is equal to E_{31}. The design scalability in this case is based on the tailoring of the big quantum well where the optical transition occurs. In order to achieve low energies with an intra-well design the active well is made several thousands of ångstrøm wide, as the transition energy scales with L^{-2}. We can then schematize our system with an infinite quantum well: since the $|3\rangle \longrightarrow |2\rangle$ oscillator strength is almost constant ($f_{32} \approx 27$, still depending on the tunnel coupling with the adjacent wells) and twice as the one for $|2\rangle \longrightarrow |1\rangle$ transition ($f_{21} \approx 14$) we rescaled the design without major modifications to the injector from 3.7 THz [65] down to 1.39 THz [66]. The issue about the scaling of the gain cross section for very long wavelengths is then related to the period length L_p and to the level broadening $2\gamma_{ij}$.

The injector energy width is rescaled accordingly to the energy E_{21}. The cross-absorption is mainly avoided by chirping the wavefunctions in the superlattice and minimizing the overlap. In the scaling procedure the sheet carrier density has been kept constant and equal to $5\times10^{10}\,\mathrm{cm}^{-2}$. The relevant quantities for the series of low energy intra-well lasers are summarized in Table 2. The structure is well described by a three level model: in order to maximize the population inversion the upper state lifetime τ_{32} has to be maximized together with the minimization of the lower state lifetime τ_2. A resonant scattering mechanism to reduce the lower state lifetime can be provided for specific values of the magnetic field which satisfy the resonance condition $E_{21} = \Delta n\hbar\omega_c$ $(n = 1, 2, 3, \ldots)$. At the same time, in order to increase the upper state lifetime the energy spacing E_{32} will be adjusted in order to have the Landau states completely off resonance, i.e. $E_{32} \neq n\hbar\omega_c$ and to minimize the scattering rate. Such a level arrangement will produce a ratio of energies $E_{32} = \frac{3}{2}E_{21}$, which has been kept for the structures emitting from 3,6 THz to 1.39 THz. This off-resonance condition is restricted to the one electron scattering processes and at the first order for the two electron processes [67]. The injection coupling $2\,\hbar\Omega$ is kept at low values of 0.2 meV and below (see Table 2). This will re-

Table 2 Summary of the characteristics for the four magnetically assisted, intra-well laser. Above the double line are calculated values and design parameters, below are measured and deduced values. SP stands for single plasmon waveguide, DM stands for double metal.

Layer	A3096	A3520	V198	A3913
$h\nu$ $\|3\rangle \to \|2\rangle$, meV	7.9	6.9	5.9	4.1
$\|4\rangle \to \|3\rangle$	–	–	9.3	–
Active well width, nm	55.0	57.0	60.7	76.5
Thickness of AR, µm	17	16.9	16.4	16.1
Number of periods	100	100	95	95
Period length, nm	170.1	169.4	173.0	170.4
Oscillator strength	29	25.5	25	25
Al fraction	0.15	0.15	0.15	0.1
Carrier density, 10^{10} cm^{-2}	5.3	5.2	5.1	4.0
Injector coupling, $2\,\hbar\Omega$	0.12	0.2	0.2	0.15
ΔE_p , meV	12.9	11.8	9.9	8.2
Waveguide	SP	SP	SP-DM	DM
$J_{\rm thr}^{\rm min}$, A/cm^2	1	4	3	11
$J_{\rm max}$, A/cm^2	40	32	20	35
$T_{\rm max}$, K	65	–	40	57
$T_{\rm max}^{4\to3}$, K	–	–	75	–

duce the leakage current due to coupling with the states $|1\rangle$ and $|2\rangle$ of the active well and also satisfy the optimal injection condition described in Sect. 2: the electroluminescence linewidth of the intra-well transition in wide quantum wells is found to be below 0.7 meV and is expected to narrow significantly with the applied magnetic field.

The properties of the lasing system will ultimately depend on the ratio between the cyclotron energy $\hbar\omega_c = \hbar eB/m^*$ and the energy dispersion ΔE_{31}, as schematized in Fig. 11a,b. When $\frac{\hbar\omega_c}{\Delta E_{31}} < 1$ the Landau levels originated from the different electronic states of the active region will be coupled by elastic scattering phenomena as electron-electron (e-e) scattering, interface roughness (IR) scattering and impurity scattering [60, 68]. When the ratio $\frac{\hbar\omega_c}{\Delta E_{31}} > 1$, Landau states are well separated in energy and only elastic resonances corresponding to many-body processes [67] and non-elastic processes [69] can be observed. The trend in this scenario will be a strong quenching of the non-radiative scattering processes due to the reduced phase space available for the diffused electrons . The strong confinement behavior in very high magnetic field ($B > 12$ T) has been analyzed in Ref. [70]: in the present paper we will concentrate our analysis up to a field of 12 T.

5.2. *Laser emission as a function of the applied field and sub-THz lasing*

The lasers are measured in an He-cooled cryostat equipped with superconducting coils allowing a maximum field of 14 T. The laser emission is either detected with an internal InSb cyclotron resonance detector or coupled outside the cryostat with a Fresnel lens of polyethylene and then fed into an FTIR equipped with an He-cooled bolometer. This setup allows to perform magnetotransport and magneto-optical characterization of the samples. A scheme of the experimental arrangement is reported in Fig. 11c. The whole set of lasers, processed in a single-plasmon waveguide configuration (see Sect. 3.1) does not show laser action without applied magnetic field. Application and sweeping of the magnetic field induces laser action with huge modulations in the emitted power and in the threshold current. The modulation in the laser emission is due to the tuning of the population inversion [64, 65] induced by the intersubband Landau scattering. In Fig. 12a is visible the laser emission as a function of the applied field for constant injected cur-

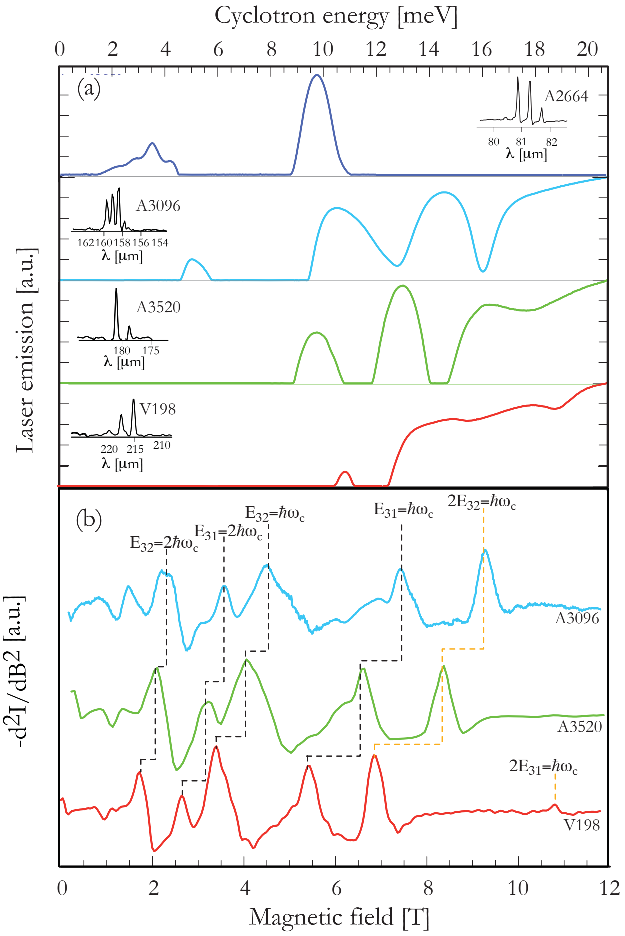

Figure 12 (online color at: www.lpr-journal.org) (a) Normalized laser emission as a function of the applied magnetic field for the five structures covering the spectral range from 3.7 THz to 1.39 THz. (b) differential transport analysis to highlight the scattering channels. Resonances due to elastic coupling between Landau states are labeled with the corresponding transition. Two-electron resonances are indicated with orange dashed lines. The measurements have been performed at 4.2 K.

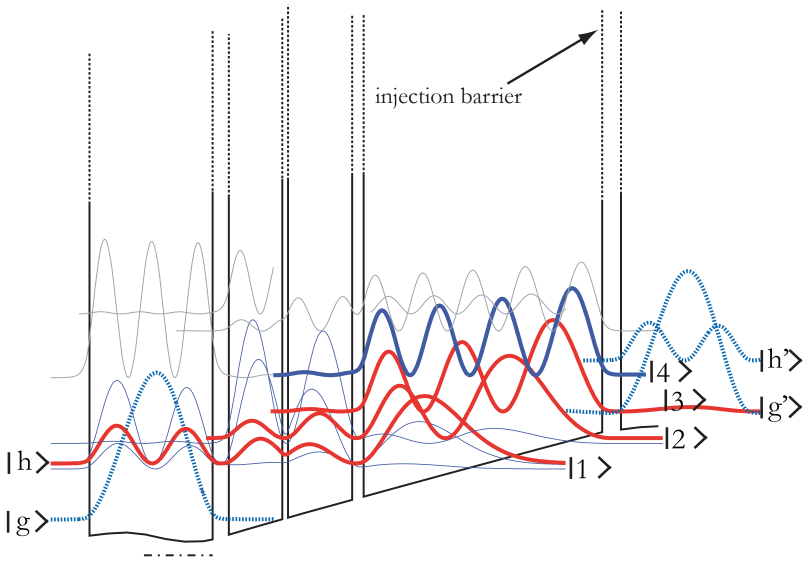

Figure 13 (online color at: www.lpr-journal.org) (a) Bandstructure for sample A3913 emitting at 950 GHz calculated at $T = 20$ K, for an applied electric field of 0.95 kV/cm. The dashed line highlights the doped region. The layer sequence, starting from the injection barrier is (in nm): **6.0** / 76.5 / **3.7** / 20.5 / **1.9** / 17.1 / **5.2** / 20.0 19.5 /. The figures in bold face represent the $Al_{0.10}Ga_{0.90}As$ barriers and the underlined layers are doped with Si, $1.9 \cdot 10^{16}$ cm^{-3} in density. This doping level yields a sheet carrier density $n_s = 4 \cdot 10^{10}$ cm^{-2}.

rent for all the series of intra-well lasers from 3.7 THz down to 1.39 THz. In Fig. 12b the transport characteristics of the lasers below 2 THz are analyzed by plotting the second derivative [71] of the current flow at constant bias as a function of the magnetic field. The resonances are then attributed to the different states of the heterostructures by comparing the cyclotron energy values to the bandstructure calculations: a very good agreement and a coherent rescaling of all the principal features is observed.

We highlight the presence of a resonance at a cyclotron energy value which equals twice the photon energy: such a resonance has been theoretically predicted and observed in transport by Kempa and co-workers [67]. This condition physically correspond to the situation where the Landau ladders are midway misaligned and the details of the electronic quasistable state in this regime are still under debate (see Ref. [72]). Energy conservation is ensured in this elastic process because two electrons are involved: one gains $+\hbar\omega_c/2$ and the other loses $-\hbar\omega_c/2$. We clearly observe this resonance on the whole ensemble of lasers of Fig. 12 in the magneto-transport as a peak in the current and as a dip in the laser emission as a consequence of the decreased population inversion.

An accurate measurement of the emitted power has not been carried out due to the uncertainties in the collection efficiency of the experimental system (see Fig. 11). Nevertheless, a rough estimate of the collected power gives values ranging in the 0.5–5 mW for the whole set of measured lasers.

A further evolution of the intra-well design has led to the structure for sub-THz lasing. As discussed extensively in Sect. 4, as the photon energy is decreased the resonant cross-absorption at the photon energy increases and structures based on dense minibands are disfavored. The injector design has to be simplified: we modified the quasi-superlattice injector of the big well design by inserting a system of coupled quantum wells that create an energy gap in the low-energy absorption spectrum of the heterostructure. We modified also the composition of the barriers which now contain only 10 % of Aluminium. The electronic bandstructure for sample A3913 is displayed in Fig. 13: it consists of four quantum wells, the energy spacing between radiative states $|3\rangle$ and $|2\rangle$ being equal to $E_{32} = 4.1$ meV. The population inversion at zero field is enhanced through the double resonance condition [19] between states $|2\rangle$ and $|1\rangle$ and the doublet of states of the adjacent system of coupled quantum wells. The last wide well (39.5 nm) completes the structure, with an energy spacing $E_{gh} = 8.5$ meV which is intended to minimize the cross absorption at the photon energy coming from the tails of the intersubband transition $|g\rangle \longrightarrow |h\rangle$. The calculated absorption profile for this structure is reported in Fig. 2 for two lattice temperatures. The doping profile is optimized by doping only a fraction of the 39.5 nm quantum well: according to the bandstructure calculation the resulting self-consistent potential allows a good resonant alignment of the whole structure. The devices are processed as double metal Fabry-Perot resonator with Au-Au wafer bonding (see Sect. 2).

A plot of the light emission as a function of the applied magnetic field and of the injected current density is displayed in Fig. 14a. Laser action starts at 5.8 T and displays two local minima at 7.54 T and 10.4 T. These minima and the other features which are observable in the transport as a function of the applied field are signatures of the intersubband Landau resonances between the states of the active well. Due to the very low current densities all the intra-well stuctures can operate in continuous wave. This enhances also the quality of the transport measurements. In Fig. 14b,c are reported transport measurements together with their second derivative in respect to the magnetic field: the differential analysis highlights the narrow resonances which can be observed for very low values of the applied magnetic field. For such a structure with low-energy separation the

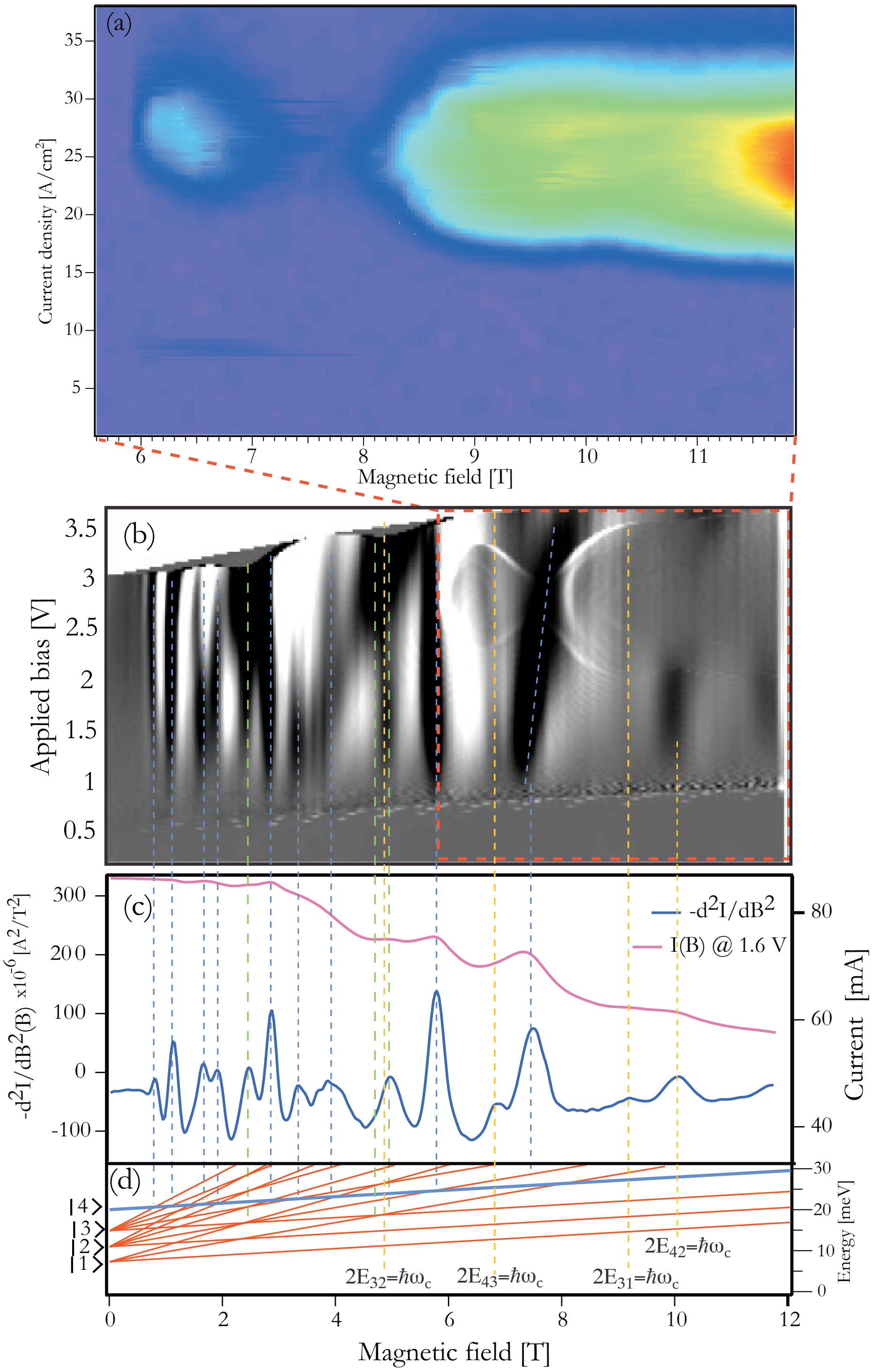

Figure 14 (online color at: www.lpr-journal.org) (a) density plot of laser emission as a function of injected current and applied magnetic field for a 320 µm × 1 mm ridge of sample A3913 ($T = 10$ K). (b) density plot of d^{2}J/dB^2 as a function of applied bias and magnetic field at 4.2 K. The red dashed box highlights the lasing region. The white feature in the lasing region corresponds to the discontinuity in the transport due to the threshold and to the stop of laser action. (c) Section of the previous graph at a constant bias together with the corresponding I(B) curve. (d) Landau Fan plot of the active region levels: resonances involving state $|4\rangle$ are marked with blue dashed lines, the ones involving state $|3\rangle$ with green dashed lines and the multi-electron resonances are indicated with orange-dashed lines.

attribution of the resonances to the states of the structures is more difficult than in higher energy devices [39]. Landau fan analysis highlights the presence of a leakage channel due to a consistent number of electrons injected in state $|h\rangle$ that can be detected by transport because they populate state $|4\rangle$. In fact the main resonances observed in the transport are due to the coupling of the level $|4\rangle$ with the other levels $|1,2,3\rangle$ of the active region. This constitutes a large leakage channel that reduces drastically the injection efficiency by resonant tunneling from state $|g\rangle$ to state $|3\rangle$. The observation of the two-electron resonances (dashed orange lines in Fig. 14) at twice the energy separation of the levels is more difficult in this sample because the quasi-triangular well leads to levels spacing very close in energy

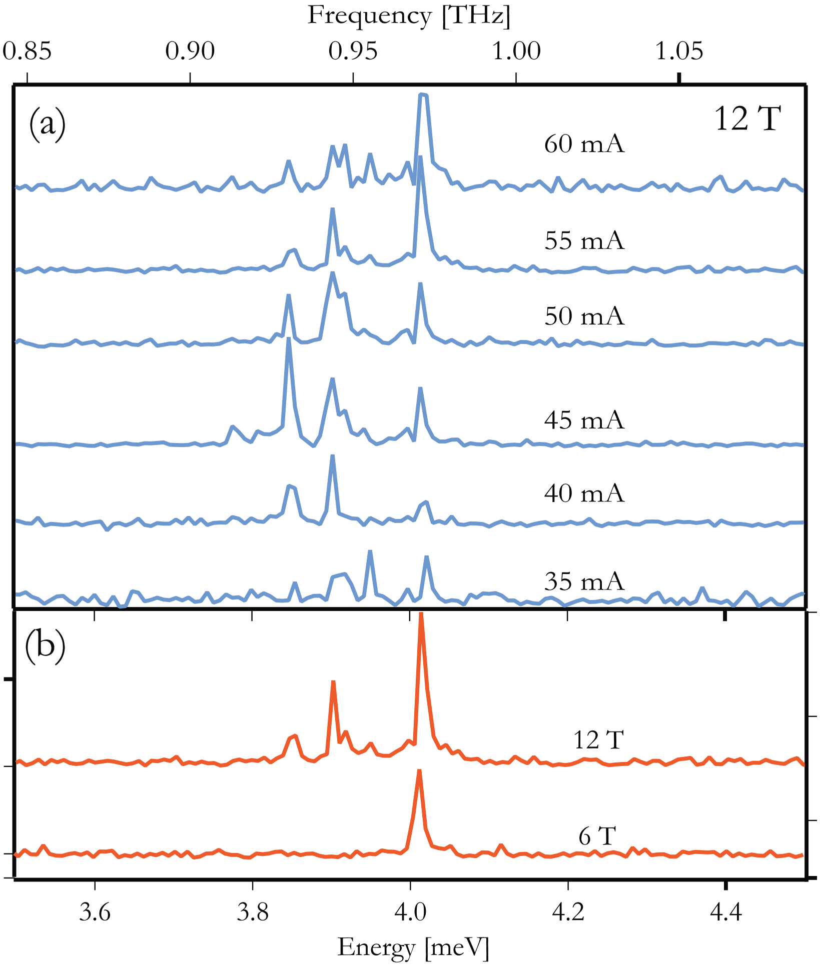

Figure 15 (online color at: www.lpr-journal.org) (a) spectral evolution of sample A3913 at 12 T for different injection currents. (b) spectral emission of sample A3913 as a function of the applied magnetic field.

$E_{32} \simeq E_{21}$ and then the condition $2E_{32} = \hbar\omega_c \approx E_{31}$. This multi-resonance conditions correspond to a field of about 4.6 T: a big feature, which broadens with the applied bias (and then with the injected current) is indeed observed at 4.6–5 T. The other 2-electron resonances are still detectable in the transport, but at higher fields a discrepancy is observed between the calculated values and the measured ones. The resonance $2E_{43} = \hbar\omega_c$ is expected at 6.48 T and is observed at 6.74 T ($\Delta E = 0.46$ meV); the one at $2E_{42} = \hbar\omega_c$ is expected at 10.56 T and is observed at 10 T ($\Delta E = 0.96$ meV). The presence of narrow resonances at very low values of the applied magnetic field is a proof of the reduced level broadening displayed by such wide-well structures. This kind of analysis also allows a mapping of the light emission features on the transport. Laser threshold and the end of the laser action are clearly observed on the differential density plot (Fig. 14b): the discontinuity at the end of the laser action, which in this case does not correspond to NDR, has been theoretically predicted and observed on other intra-well structures [19]. It is interesting to note that the measurement of Fig. 14b,c are performed on a very small Fabry-Perot double metal ridge (550 × 100 µm) without any change in the threshold current density in respect to wider devices. The dynamic range of the laser increases as a function of the applied magnetic field reaching 67 % at 12 T. The threshold current density is 25 A/cm^2 at 5.8 T and reaches its minimum value of 11.5 A/cm^2 at $B = 12$ T. Compared to previous devices at shorter wavelengths the threshold current density in the strong confinement regime is one order of magnitude higher. This sizeable difference can be ascribed to the leakage current which is injected in the active well via state $|h\rangle$. The laser is operating up to 57 K in pulsed, a plot of the temperature dependence of the threshold as a function of the applied field is reported in the inset of Fig. 16. In Fig. 15 is reported the spectral emission for sample A3913 as a function of the applied magnetic field. As the lifetime ratio is enhanced via magnetic confinement, enough gain to overcome the losses is present on a wider spectral range, spanning a window of width ≈ 0.2 meV at the maximum injected current value/ applied magnetic field. The lowest frequency lasing mode is observed at 930 GHz.

5.3. Ultra-low threshold current operation

In Fig. 16 are reported the threshold current densities as a function of the applied field for the four samples emitting

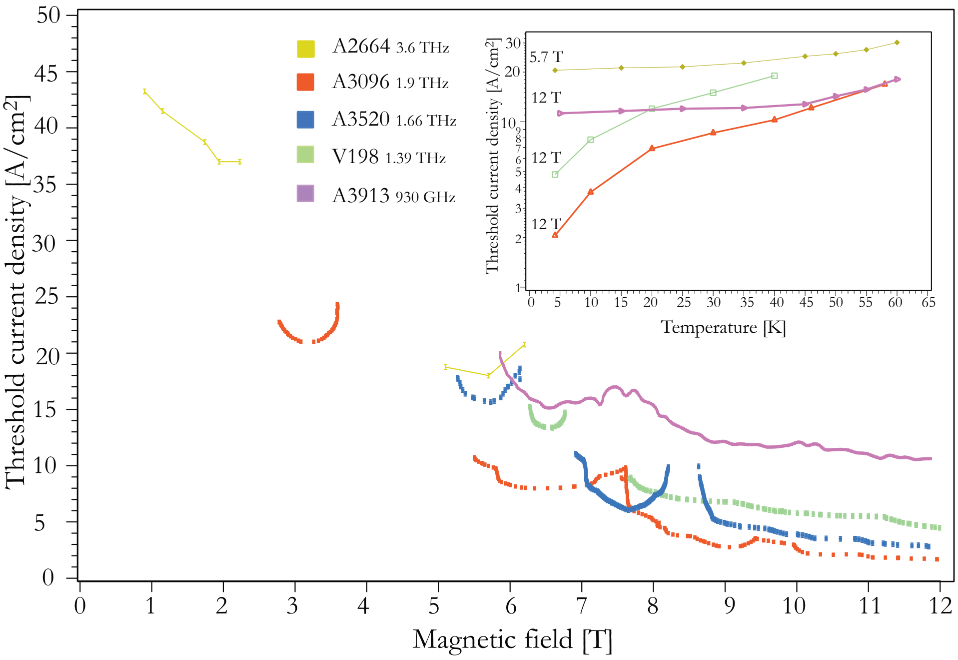

Figure 16 (online color at: www.lpr-journal.org) Threshold current density for all the intra-well samples investigated at $T = 4.2$ K. The sample A2664 emitting at 3.6 THz is not in the strong confinement regime and its minimum value of the threshold current is a factor of 10 higher than the other samples. The sample A3913 emitting at 950 GHz shows threshold current density values higher than the other strong confinement samples. Inset: temperature dependence of the threshold current density for samples A2664, A3096, V198 and A3913 at the magnetic field intensity corresponding to the maximum operating temperature.

below 2 THz and also the data for sample A2664 which is based on the same design but emits at 3.6 THz, as a comparison. On the threshold current density we can observe the same oscillations which are present in the light emission. As discussed in Sect. 5.1 the lasing regime changes when the system enters the strong confinement region, as shown in Fig. 16. The threshold current density drops by a factor of five when $\hbar\omega_c > \Delta E_{31}$. This is not true for sample A2664 for which the strong confinement limit is set at $B = \frac{m^* \Delta E_{31}}{\hbar e} \approx 14.5$ T. The threshold in the strong confinement region reduces to values below 5 A/cm^2 , which are the lowest measured for any intersubband laser.

We believe that the observed ultra-low threshold current densities are due to two main effects. The first one is the increase in intersubband lifetime as a function of the applied magnetic field: this has been observed in the transport characteristics of intersubband emitters based on a diagonal transition of Ref. [73] , and from the reduction in the dynamic range of THz lasers as a function of the applied magnetic field. We can claim an increase of the lifetime of the upper state τ_{up} from the positive magnetoresistance observed on all our laser samples in magnetic field [70]. From the model illustrated in Sect. 2 the current flow is regulated by the upper state lifetime $\tau_{\mathrm{up}}(B)$ which governs $J_{\max}(B)$. The second main effect of the magnetic confinement is on the intra-subband dephasing. This dephasing, which contributes substantially to the linewidth profile, is also efficiently quenched by the magnetic field: electroluminescence measurements in magnetic field [63, 68] report a strong narrowing of the THz emission with increasing field. The electron localization induced by the magnetic field and the disorder at the interfaces reduces the intra-Landau level scattering rate. This narrowing of the transition leads to an enhanced value for the gain (see Eq. (4)) and also to an improved injection in the active well by the increase of the term $4|\Omega|^2\tau_\perp\tau_{\mathrm{up}}$. The narrowing of the intersubband linewidth leads also to a reduction of the waveguide losses by reducing the cross-absorption in the tails of the intersubband transition in the injector region [39].

The temperature behavior of the threshold current density for the intra-well samples in high magnetic field is indicative of the peculiar regime of operation where the carriers are confined on by disorder-induced potential on interface "boxes" [39]. In the inset of Fig. 16 are reported the threshold current densities as a function of the lattice temperature at magnetic fields corresponding to the highest operating temperatures for the different lasers. Sample A2664 is not in the strong confinement regime ($\Delta E_p = 25$ meV), and the low temperature behavior of the threshold current follows the usual trend of THz QC lasers (see Fig. 7). On the contrary, the curves relative to samples A3096 and V198 show the typical activated behavior which is ascribed to a disorder induced localization potential with an activation energy of about 1 meV [39]. The curve relative to sample A3913 does not show this activated behavior even if the sample is in the strong confinement regime. The value of the threshold current density is also a factor of 5 higher in respect to the other two samples. We explain this different behavior with the leakage current channel constituted by the state $|h\rangle$, as already discussed in the previous paragraph.

As observed in the bound-to-continuum samples, the maximum operating temperature seems not the be directly related to the photon energy. With the exception of sample V198 which displayed a $T_{\max} = 40$ K, all the other samples lase in pulsed operation up to a temperature of 55–65 K. The fact that the maximum operating temperature is roughly independent from the photon energy can indicate that the main mechanism responsible of the degradation of

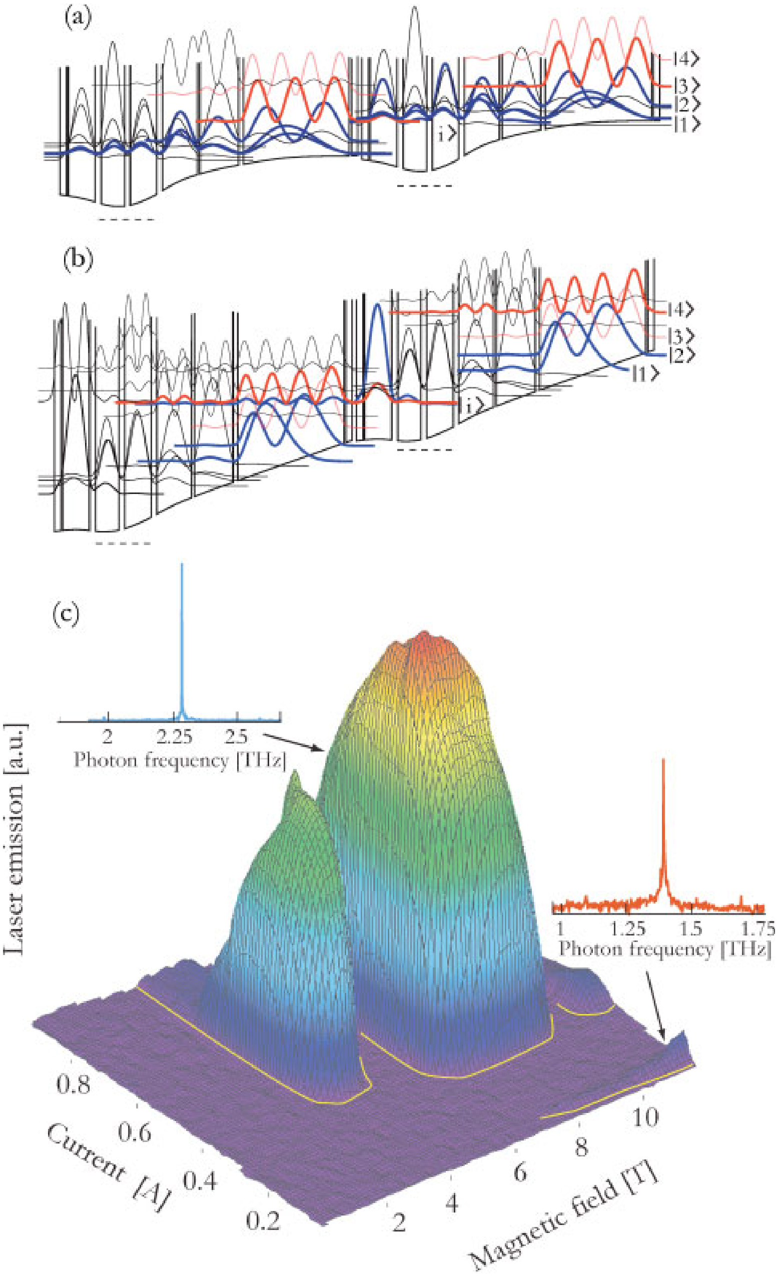

Figure 17 (online color at: www.lpr-journal.org) (a) Bandstructure for sample V198 aligned on the $|3\rangle \longrightarrow |2\rangle$ transition. The dashed line highlights the doped region. (b) bandstructure for sample V198 aligned on the $|4\rangle \longrightarrow |3\rangle$ transition. (c) Three dimensional graph showing laser emission as a function of injected current and applied magnetic field. The laser emission is plotted in log scale in order to enhance the low intensity emission for the laser line at 1.39 THz. The yellow curve tracks the threshold current as a function of the applied magnetic field. The measurements are performed at $T = 4.2$ K.

the laser is not the thermally activated emission of optical phonons from electrons lying in the upper state [6]. In fact the phonon emission should be efficiently quenched by the magnetic field [60].

5.4. *Multi-wavelength operation and lasing on excited states without magnetic field*

Multiwavelength operation can also be achieved in such intra-well structures by selectively injecting carriers in one of the excited states of the active quantum well [74]. As shown schematically in Fig. 17a,b, we inject carriers in states $|3\rangle$ or $|4\rangle$ by resonant tunnelling depending on the applied bias. Emission is then achieved at frequencies corresponding to 3→2, 4→3 transitions respectively [66]. A plot of the light emission as a function of the applied magnetic field in the 0–12 T interval for sample V198 is reported in Fig. 17c. Two distinct regions are evident: at high injection currents ($I > 0.4$ A) and starting from an applied magnetic field value of 3 T a strong laser emission is detected, which indeed corresponds to the $|4\rangle \rightarrow |3\rangle$ transition. At higher magnetic fields ($B > 7$ T) and low injection currents we can observe the laser emission relative to the $|3\rangle \longrightarrow |2\rangle$ transition. The laser emission is then cleanly electrically switchable between two widely spaced frequencies. The light emission has been plotted in logarithmic scale in order to account for the large intensity variations between the two

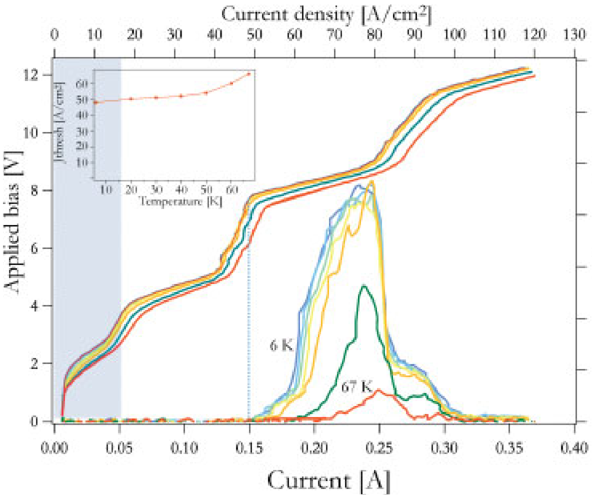

Figure 18 (online color at: www.lpr-journal.org) Pulsed L-I-V characteristics of sample V198 in a double metal waveguide (1 mm × 320 µm) as a function of the temperature at $B = 0$. The clear steps in the I-V characteristics correspond to the successive alignments on the excited states of the wide active quantum well. The light blue area corresponds to the injection in state $|3\rangle$. Inset: temperature dependence of the threshold current density.

regions. This intensity difference is due to the higher outcoupling from the waveguide for the shorter wavelength and to the higher injected current values (the current density differs by a factor of ten). The highest operating temperature for the $|4\rangle \rightarrow |3\rangle$ is 75 K at 7.5 T applied magnetic field.

The sample was also processed in a double-metal waveguide configuration. Interestingly, the increased figure of merit of the double metal waveguide leads to laser action *without* applied magnetic field on the shorter wavelength ($|4\rangle \rightarrow |3\rangle$, 2.3 THz) transition. The performance of such a laser in the new waveguide configuration are reported in Fig. 18. The transport clearly shows the successive alignment of the confined states in the large quantum well with the injector. Threshold is reached for a current density of about 50 A/cm^2 which is still a very low value for this frequency. Careful inspection of the I-V characteristics reveals that even without applied magnetic field laser threshold is achieved as soon as the alignment on the level 4 is reached (dashed line). In this case the population inversion is achieved by a mixture of resonant tunneling and scattering between the closely spaced levels $|1, 2, 3\rangle$. The temperature dependence of the laser threshold is very similar to what observed in magnetic field, with a $T_{\text{max}} = 67$ K. Despite the low threshold current density, the devices did not show CW laser action, probably due to the high value of the electric field which can eventually create instabilities and field domains in a wide well structure when injecting from a dense miniband. Such a laser architecture can represent an interesting system for studying gain at THz frequencies in a relatively simple structure. The use of transitions between excited states increases the oscillator strength due to the intersubband sum rule [13]: such structures, as the one presented here, would show very low threshold current densities, although as the energy spacing of the quantum well levels would approach the LO phonon value drastic reduction of the upper state lifetime would be expected.

6. Perspectives and conclusions

The data presented in this paper show the possibility to selectively inject carriers in quantum states which present an energy separation of 1 THz and below. These states can be clearly resolved in transport and laser emission has been achieved between them. What limits we can expect on wavelength and operating temperatures for those lasers? From the point of view of the optical resonator we discussed in Sect. 2 that the figure of merit of the double metal waveguide scales favorably with the frequency. The losses coming from free carrier absorption in the active region can be engineered; the contribution coming from the doped regions of the cladding can be also minimized.

We believe that the broadening of the states is what will ultimately limit the realization of high temperature THz lasers with intersubband transitions. The interface roughness scattering is believed to represent the major source of transition broadening. The scaling of the quantum wells width and the use of structures with low Al content substantially reduces the efficiency of this scattering mechanism. As demonstrated with our devices from transport data with and without applied magnetic field, the levels are narrow enough to allow selective injection with energy separation below 4 meV.

The possibility to achieve high temperature operation of such low frequency devices is related to the ability to reduce the leakage current prior to alignment in order to fully exploit the dynamic range. The injection process can be also very sensitive to the level broadening induced by the presence of the dopants. It is worth to mention that the substantial difference in electronic temperature between active region and injector reported for bound-to-continuum devices [69, 75] can affect also the injection process. A possible way to circumvent this problem would be to rely on a different type of injection scheme which allows to further extend the dynamic range.

To summarize, in this paper we reported about two different quantum cascade laser designs operating in the low THz spectral region. The scaling of the structures, which is a key ingredient of the quantum cascade approach, is fully exploited to obtain laser action over a wide spectral window. The bound-to-continuum with split injector design shows very good performance with pulsed operation up to 100 K and a pronounced Stark tuning of the gain curve that can be proficiently used in several applications. The magnetically assisted gain structures probe the limits of the quantum cascade approach: a control over the in plane degree of freedom demonstrates the possibility of extreme reduction of the threshold current density reaching limits as low as 1 A/cm^2 and photon energies below 4 meV.

Acknowledgements Financial support from Swiss National Science Foundation through the NCCR project and from EU community through the IP TERANOVA are gratefully acknowledged. Part of the work was done at University of Neuchâtel, Neuchâtel, Switzerland.

Giacomo Scalari got his diploma in Physics at the Università di Pisa, Italy in 1999 working on magnetic resonance force microscopy. After a period at Scuola Superiore S. Anna, Pisa, in 2001 he joined the research group of Prof. Jérôme Faist at the University of Neuchâtel, Switzerland. There, he completed his PhD in 2005 with a thesis on magneto-spectroscopy and development of THz quantum cascade lasers. After two years of Post-Doc he is currently Associate Researcher in the group of Prof. Faist at ETH Zuerich. He received the 2006 Swiss Physical Society award for Applied Physics.

Christoph Walther was born in Switzerland in 1979. He received the M. S. degree in physics from University of Neuchâtel, Switzerland, in 2005, where his studies focused on the investigation of magneto-transport and electroluminscence of a terahertz quantum cascade emitter. He is currently working towards the Ph.D. degree. He joined the group of Prof. Faist in March 2005, where he is working on the developement of low frequency quantum cascade lasers.

Milan Fischer obtained his degree in Physics from the Charles University in Prague in 2004. Currently he is working towards his Ph. D. at the ETH Zurich concentrating on the growth and development of Terahertz Quantum Cascade lasers.

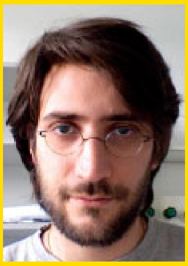

Romain Terazzi was born in 1978, studied physics at the University of Neuchâtel, Switzerland. He is currently doing his Ph. D. in the group of Prof. Faist at ETH Zurich on simulation of quantum cascade lasers.

Harvey E. Beere received the M. Eng. degree in electrical and electronic engineering from Imperial College, London, UK in 1993, and the Ph. D. degree in physics from the University of Cambridge, Cambridge, UK, in 1999. He is currently a Senior Research Associate in the Semiconductor Physics Group at the Cavendish Laboratory, University of Cambridge, where his work has concentrated on the growth and development of novel electrical and optical semiconductor devices, including quantum cascade lasers.

David A. Ritchie received the first degree in physics from the University of Oxford, UK, in 1980, and the D. Phil. degree in the physics of liquid helium from the University of Sussex, Brighton, UK, in 1985. He is a Professor of experimental physics and the Head of the Semiconductor Physics Group, Cavendish Laboratory, University of Cambridge, UK He has been engaged in the fields of IIIV semiconductor physics and has extensive experience of the growth, fabrication, and measurement of lowdimensional electronic and optical structures. He is the author or coauthor of more than 650 papers. Prof. Ritchie was awarded the 2008 Tabor Medal and Prize by the UK Institute of Physics for distinguished research in surface or nanoscale physics.

Jèrôme Faist was born in Geneva, and obtained his Bachelor and Ph. D. in Physics, in the group of Prof. F.-K. Reinhart from the Swiss Institute of Technology in Lausanne in 1985, 1989 respectively. After a post-doc in IBM Rueschlikon (89–91), he joined F. Capasso's group in Bell Laboratories in 1991 where he worked first as a post-doc and then as a Member of Technical Staff. From 1997 to 2007, he was professor in the physics institute of the University of Neuchâtel. In 2007, he became professor in the Institute for Quantum Electronics of the ETH Zurich. His central role in the invention and first demonstration of the quantum cascade (QC) laser in 1994 was recognized by the IEE premium (1995), the IEEE/LEOS William Streifer award (1998), the Michael Lunn award (1999), the ISCS "Young scientist award" (1999), and the Swiss National Latsis Prize (2003).

References

[1] P. Siegel, IEEE Trans. Microw. Theory Tech. **50**(03), 910–928 (2002).

[2] M. Tonouchi, Nature Photonics **1**, 97–105 (2007).

[3] J. Faist, F. Capasso, D. Sivco, C. Sirtori, A. Hutchinson, and A. Cho, Science **264**, 553–556 (1994).

[4] L. Diehl, D. Bour, S. Corzine, J. Zhu, G. Höfler, M. Loncar, M. Troccoli, and F. Capasso, Appl. Phys. Lett. **88**, 201115-1–3 (2006).

[5] A. Mohan, A. Wittmann, A. Hugi, S. Blaser, M. Giovannini, and J. Faist, Opt. Lett. **32**, 2792–2794 (2007).

[6] B. S. Williams, Nature Photonics **1**, 517–525 (2007).

[7] M.A.Belkin, M.J. Fan, S. Hormoz, F. Capasso, S. Khanna, M. Lachab, A. Davies, and E. Lindfield, Opt. Express **16**(05), 3242–3248 (2008).

[8] A. Lee, Q. Qin, S. Kumar, B. Williams, Q. Hu, and J. Reno, Appl. Phys. Lett. **89**, 141125-1–3 (2006).

[9] H. Hübers, S. Pavlov, H. Richter, D. Semenov, L. Mahler, A. Tredicucci, H. Beere, and D. Ritchie, Appl. Phys. Lett. **89**, 061115-1–3 (2006).

[10] J. Gao, J. Hovenier, Z. Yang, J. Baselmans, A. Baryshev, M. Hajenius, T. Klapwijk, A. Adam, T. Klaassen, B. Williams, S. Kumar, Q. Hu, and J. Reno, Appl. Phys. Lett. **86**, 244104-1–3 (2005).

[11] L. Sirigu, A. Rudra, E. Kapon, M.I. Amanti, G. Scalari, and J. Faist, Appl. Phys. Lett **92**, 181111-1–3 (2008).

[12] R. Köhler, A. Tredicucci, F. Beltram, H. Beere, E. Linfield, A. Davies, D. Ritchie, R. Iotti, and F. Rossi, Nature **417**, 156–159 (2002).

[13] C. Sirtori, F. Capasso, J. Faist, and S. Scandolo, Phys. Rev. B **50**(12), 8663–8674 (1994).

[14] L. Ajili, G. Scalari, N. Hoyler, M. Giovannini, and J. Faist, Appl. Phys. Lett. **87**, 141107-1–3 (2005).

[15] M. Vitiello, G. Scamarcio, V. Spagnolo, B. Williams, S. Kumar, Q. Hu, and J. Reno, Appl. Phys. Lett. **86**, 111115-1–3 (2005).

[16] R. Kazarinov and R. Suris, Sov. Phys.-Semicond. **6**(1), 120–131 (1972).

[17] C. Sirtori, F. Capasso, J. Faist, A. Hutchinson, D. Sivco, and A. Cho, IEEE J. Quantum Electron. **34**(9), 1722–1729 (1998).

[18] S. Lee and A. Wacker, Appl. Phys. Lett. **83**(13), 2506–2508 (2003).

[19] G. Scalari, R. Terazzi, M. Giovannini, N. Hoyler, and J. Faist, Appl. Phys. Lett. **91**, 032103-1–3 (2007).

[20] H.Callebaut and Q. Hu, J. Appl. Phys. **98**, 104505-1–11 (2005).

[21] R. Green, A. Tredicucci, L. Mahler, N. Vinh, B. Murdin, C. Pidgeon, H. Beere, and D. Ritchie, in: Proceedings of ITQW 07, Ambleside, Cumbria, UK (2007).

[22] T. Unuma, M. Yoshita, T. Noda, H. Sakaki, and H. Akiyama, J. Appl. Phys. **93**(3), 1586–1597 (2003).

[23] C. Worrall, J. Alton, M. Houghton, S. Barbieri, H. Beere, D. Ritchie, and C. Sirtori, Opt. Express **14**(1), 171–181 (2006).

[24] S. Kumar, B. Williams, Q. Hu, and J. Reno, Appl. Phys. Lett. **88**, 121123-1–3 (2006).

[25] C. Walther, G. Scalari, J. Faist, H. Beere, and D. Ritchie, Appl. Phys. Lett. **89**, 231121– (2006).

[26] J. Faist, F. Capasso, C. Sirtori, D. Sivco, and A. Cho, Quantum cascade lasers, in: Intersubband transitions in quantum wells: Physics and device applications II, edited by H. Liu and F. Capasso (Academic Press, 2000), Chap. 1, pp. 1–83.

[27] F. Banit, S. Lee, A. Knorr, and A. Wacker, Appl. Phys. Lett. **86**, 41108-1–3 (2005).

[28] R. Terazzi, T. Gresch, M. Giovannini, N. Hoyler, N. Sekine, and J. Faist, Nature Phys. **03**(05), 329–333 (2007).

[29] J.Kroll, J.Darmo, S.Dhillon, X. Marcadet, M. Calligaro, C. Sirtori, and K. Unterrainer, Nature **449**, 698–701 (2007).

[30] H. Luo, S. Laframboise, Z. Wasilewski, G. Aers, H. Liu, and J. Cao, Appl. Phys. Lett. **90**, 041112-1–3 (2007).

[31] L. Sirigu, R. Terazzi, M. I. Amanti, M. Giovannini, J. Faist, L. A. Dunbar, and R. Houdré, Opt. Express **16**(08), 5206–5217 (2008).

[32] L. Dunbar, V. Moreau, R. Ferrini, R. Houdré, L. Sirigu, G. Scalari, M. Giovannini, N. Hoyler, and J. Faist, Opt. Express **13**(22), 8960–8968 (2005).

[33] O. Demichel, L. Mahler, T. Losco, C. Mauro, R. Green, A. Tredicucci, J. Xu, F. Beltram, H. E. Beere, D. A. Ritchie, and V. Tamosinuas, Opt. Express **14**(12), 5335–5345 (2006).

[34] Y. Chassagneux, R. Colombelli, S. Barbieri, C. Sirtori, H. Beere, and D. Ritchie, in: Proceedings of CLEO-QELS 2008, San Jose, CA, USA, 2008.

[35] H. Zhang, L. A. Dunbar, G. Scalari, R. Houdré, and J. Faist, Opt. Express **15**(25), 16818–16827 (2008).

[36] J. Ulrich, R. Zobl, N. Finger, K. Unterrainer, G. Strasser, and E. Gornik, Physica B **272**, 216–218 (1999).

[37] S. Kohen, B. Williams, and Q. Hu, J. Appl. Phys. **97**, 053106-1–9 (2005).

[38] L. Ajili, G. Scalari, J. Faist, H. Beere, E. Linfield, D. Ritchie, and G. Davies, Appl. Phys. Lett. **85**(18), 3986–3988 (2004).

[39] G. Scalari, S. Blaser, J. Faist, H. Beere, E. Linfield, D. Ritchie, and G. Davies, Phys. Rev. Lett. **93**, 237403-1–4 (2004).

[40] M. Ordal, R. Bell, R. Alexander, L. Long, and M. Querry, Appl. Opt. **26**(4), 744–752 (1987).

[41] K. Unterrainer, R. Colombelli, C. Gmachl, F. Capasso, H. Hwang, A. Sergent, D. Sivco, and A. Cho, Appl. Phys. Lett. **80**(17), 3060–3062 (2002).

[42] A. Lee, Q. Qin, S. Kumar, B. S. Williams, Q. Hu, and J. L. Reno, Opt. Lett. **32**, 2840–2842 (2007).

[43] M. Amanti, M. Fischer, C. Walther, G. Scalari, and J. Faist, IEE Elect. Lett. **43**(10), 573–574 (2007).

[44] J. Pankove, Optical Processes in Semiconductors (Dover Publications, Inc., New York, 1971).

[45] J. Faist, M. Beck, T. Aellen, and E. Gini, Appl. Phys. Lett. **78**(2), 147–149 (2001).

[46] G. Scalari, L. Ajili, J. Faist, H. Beere, E. Linfield, D. Ritchie, and G. Davies, Appl. Phys. Lett. **82**(19), 3165–3167 (2003).

[47] C. Walther, M. Fischer, G. Scalari, R. Terazzi, N. Hoyler, and J. Faist, Appl. Phys. Lett. **91**, 131122-1–3 (2007).

[48] P. Hyldgaard and J. Wilkins, Phys. Rev. B **53**(11), 6889–6892 (1996).

[49] S. Blaser, L. Diehl, M. Beck, J. Faist, U. Oesterle, J. Xu, S. Barbieri, and F. Beltram, IEEE J. Quantum Electron. **37**(3), 448–455 (2001).

[50] J. Faist, F. Capasso, C. Sirtori, D. Sivco, A. Hutchinson, and A. Cho, Nature **387**, 777–782 (1997).

[51] J. Faist, F. Capasso, C. Sirtori, D. Sivco, A. Hutchinson, S. Chu, and A. Cho, Appl. Phys. Lett. **65**(1), 94–96 (1994).

[52] S. Sze, Modern Semiconductor Device Physics (John Wiley & Sons, Inc., New-York, 1998).

[53] A. Benz, G. Fasching, A. Andrews, M. Martl, K. Unterrainer, T. Roch, W. Schrenk, S. Golka, and G. Strasser, Appl. Phys. Lett. **90**, 101107-1–3 (2007).

[54] H. Callebaut, S. Kumar, B. Williams, Q. Hu, and J. Reno, Appl. Phys. Lett. **84**(05), 645–647 (2004).

[55] L. Pfeiffer, F. Schubert, K. W. West, and C. W. Magee, Appl. Phys. Lett. **58**(20), 2258 (1991).

[56] Y. Arakawa and H. Sakaki, Appl. Phys. Lett. **40**(11), 939–941 (1982).

[57] R. Ferreira, Phys. Rev. B **43**(11), 9336–9338 (1991).

[58] D. Smirnov, C. Becker, O. Drachenko, V. Rylkov, H. Page, J. Leotin, and C. Sirtori, Phys. Rev. B **66**, 121305-1–4 (2002).

[59] C. Becker, C. Sirtori, O. Drachenko, V. Rylkov, D. Smirnov, and J. Leotin, Appl. Phys. Lett. **81**(16), 2941–2943 (2002).

[60] A. Leuliet, A. Vasanelli, A. Wade, G. Fedorov, D. Smirnov, G. Bastard, and C. Sirtori, Phys. Rev. B **73**, 085311-1–9 (2006).

[61] M. Raikh and T. Shabazyan, Phys. Rev. B **49**(8), 5531–5540 (1994).

[62] J. Ulrich, R. Zobl, K. Unterrainer, G. Strasser, and E. Gornik, Appl. Phys. Lett. **76**(1), 19–21 (2000).

[63] S. Blaser, M. Rochat, M. Beck, D. Hofstetter, and J. Faist, Appl. Phys. Lett. **81**(1), 67–69 (2002).

[64] J. Alton, S. Barbieri, J. Fowler, H. Beere, J. Muscat, E. Linfield, D. Ritchie, G. Davies, R. Köhler, and A. Tredicucci, Phys. Rev. B **68**, 081303-1–4 (2003).

[65] G. Scalari, S. Blaser, L. Ajili, J. Faist, H. Beere, E. Linfield, D. Ritchie, and G. Davies, Appl. Phys. Lett. **83**(17), 3453–3455 (2003).

[66] G. Scalari, C. Walther, J. Faist, H. Beere, and D. Ritchie, Appl. Phys. Lett. **88**(14), 141102-1–3 (2006).

[67] K. Kempa, Y. Zhou, J. Engelbrecht, P. Bakshi, H. Ha, J. Moser, M. Naughton, J. Ulrich, G. Strasser, E. Gornik, and K. Unterrainer, Phys. Rev. Lett. **88**(22), 226803-1–4 (2002).

[68] J. Ulrich, R. Zobl, W. Schrenk, G. Strasser, K. Unterrainer, and E. Gornik, Appl. Phys. Lett. **77**(13), 1928–1930 (2000).

[69] N. Péré-Laperne, L. A. de Vaulchier, Y. Guldner, G. Bastard, G. Scalari, M. Giovannini, J. Faist, A. Vasanelli, S. Dhillon, and C. Sirtori, Appl. Phys. Lett. **91**, 062102–1062102-3 (2007).

[70] G. Scalari, C. Walther, L. Sirigu, M. Sadowski, H. Beere, D. Ritchie, N. Hoyler, M. Giovannini, and J. Faist, Phys. Rev. B **76**, 115305-1–7 (2007).

[71] D. Smirnov, O. Drachenko, J. Leotin, H. Page, C. Becker, C. Sirtori, V. Apalkov, and T. Chakraborty, Phys. Rev. B **66**, 125317-1–4 (2002).

[72] R. Ferreira, G. Bastard, C. Sirtori, G. Strasser, and K. Unterrainer, Phys. Rev. B **76**, 165322-1–5 (2007).

[73] S. Blaser, M. Rochat, M. Beck, J. Faist, and U. Oesterle, Phys. Rev. B **61**(12), 8369–8374 (2000).

[74] C. Sirtori, A. Tredicucci, F. Capasso, J. Faist, D. Sivco, A. Hutchinson, and A. Cho, Opt. Lett. **23**(6), 463–465 (1998).

[75] M. S. Vitiello, G. Scamarcio, G. Scalari, C. Walther, J. Faist, H. Beere, D. Ritchie, and V. Spagnolo, in: Proceedings of CLEO-QELS 2008, San Jose, CA, USA, 2008.